The earliest circadian clock in the mammalian brain emerges in the embryonic choroid plexus

Hélène Vitet [1], Vuong Hung Truong [1], Jihwan Myung [1,2,*]

[1] Laboratory of Braintime, Graduate Institute of Mind, Brain and Consciousness (GIMBC), Taipei Medical University, New Taipei City 235, Taiwan

[2] Graduate Institute of Medical Sciences (GIMS), College of Medicine, Taipei Medical University, Taipei 110, Taiwan

[*] Correspondence: Jihwan Myung (jihwan@tmu.edu.tw)

Abstract

Maternal chronodisruption is linked to miscarriages and neurodevelopmental risks, yet the earliest brain circadian oscillator in the embryo and the mechanism of its emergence remain unknown. Using bioluminescent reporters for PER2 and *Bmal1*, we tracked the onset of autonomous ~24 h oscillations *ex vivo*. While the suprachiasmatic nucleus (SCN) is widely considered the first circadian structure at embryonic day (E) 14.5-15.5, we find that the fourth ventricle choroid plexus (4VCP) exhibits PER2 oscillations by E11.5-E12.5. These oscillations show hallmarks of a saddle-node on an invariant circle (SNIC) bifurcation, characterized by an initially long period converging toward 24 h and pronounced sensitivity to sub-degree temperature cycles mimicking physiological maternal cues. Transcriptional profiling of maternal and embryonic 4VCPs unveiled three epochs in clock gene expression that parallel tissue differentiation. We identify the 4VCP as the earliest detectable brain circadian oscillator, and

demonstrate how its bifurcation dynamics allow the nascent clock to couple to maternal rhythms.

Keywords: circadian clock ontogeny, choroid plexus, maternal-fetal interaction, SNIC bifurcation, embryonic brain development, temperature entrainment, suprachiasmatic nucleus

Introduction

Circadian clocks are autonomous pacemakers that align physiological processes with Earth's 24-h cycle, maintained by a robust transcription-translation feedback loop (TTFL). The transcription factors BMAL1 and CLOCK heterodimerize to activate the transcription of negative feedback components, including the *Period* (*Per1/2/3)* and *Cryptochrome* (*Cry1/2*) genes. The resulting PER and CRY proteins accumulate, form complexes, and undergo post-translational modifications that introduce a delay that sets the circadian timescale. These complexes translocate into the nucleus to repress their own transcription to complete the loop. The transcription of *Bmal1* is further regulated by REV-ERB and ROR, conferring additional robustness to the oscillation. The assemblage of these loops creates tissue-specific phase organization of clock gene expression (Myung et al., 2025). In adult mammals, the suprachiasmatic nucleus (SCN) in the hypothalamus acts as the central clock, synchronizing peripheral clocks throughout the body (Finger et al., 2020). Understanding when and how this system first emerges during development is important, as maternal chronodisruption is associated with preterm birth, miscarriage, and adverse neurodevelopmental outcomes (Astiz and Oster, 2021); yet, neither the identity nor the onset mechanism of the earliest embryonic brain clock has been established.

Circadian rhythms have been detected prenatally in humans, non-human primates, and rodents (Serón-Ferré et al., 2012; Landgraf et al., 2014). However, detection is technically challenging, due to low-amplitude oscillations and tissue-specific differences in clock gene expression. Although *Per* and *Bmal1* show no clear rhythms in whole-embryo preparations (E10-E17) (Cao et al., 2022; Dolatshad et al., 2010; Serón-Ferré et al., 2012), circadian rhythmicity of PER2 has been detected in the SCN *ex vivo* around E14.5 to E15.5 (Wreschnig et al., 2014; Carmona-

Alcocer et al., 2018). Whether the SCN is truly the first circadian structure in the embryonic brain, however, has not been systematically examined.

A strong candidate for an even earlier clock is the choroid plexus (CP). In adult mice, the CP acts as a robust clock capable of entraining the SCN through a diffusive pathway (Myung et al., 2018). This non-neuronal tissue lines the brain ventricles and filters blood to produce cerebrospinal fluid (CSF) and a distinct secretome (Saunders et al., 2023; Chau et al., 2015; Courtney et al., 2025; Edelbo et al., 2023). Among the CPs, the fourth ventricle CP (4VCP) is the first to develop, arising from the lower rhombic lip as early as E9.5, expressing *Wnt1*, *Ttr*, and *Kcne2*, with development rate peaking at E11-E12.5 (Lun et al., 2015; Hunter and Dymecki, 2007). By E14, the 4VCP becomes anatomically apparent and is thought to be differentiated, although proliferation continues postnatally (Lun et al., 2015).

Beyond mechanical support, CSF is a key volumetric regulator of early brain development. Embryonic CSF is present at neural tube closure (E9.5), initially derived from enclosed amniotic fluid before transitioning to CP-produced fluid between E10.5 and E14.5 (Chau et al., 2015). Because CP-derived volume transmission dominates early brain-wide signaling (E10.5-E11.5) and the adult CP secretome is under circadian control (Edelbo et al., 2023), an embryonic CP clock could provide early time cues for neural progenitor programs (Miyan et al., 2003; Martin et al., 2009; Gato et al., 2005).

How might such a clock emerge? The early embryo operates on timescales of hours for cell division and somitogenesis, far shorter than the 24 h cycle, and an abrupt transition from the “somitogenesis era” to the “circadian era” has been proposed (Caviness et al., 1995; Yagita, 2024). From a nonlinear dynamics perspective, a quiescent state can transition to stable

oscillation through a bifurcation. Circadian clocks, along with many oscillations in biology, are often modelled as a supercritical Hopf bifurcation, in which amplitude grows gradually while the period remains constant (Murayama et al., 2017). However, developmental transitions, such as the onset of the first heartbeat in zebrafish, can arise via a noisy saddle-node on an invariant circle (SNIC) bifurcation (Jia et al., 2023). A SNIC produces finite amplitude oscillations abruptly, with an initially long period that shortens toward ~24 h. Near threshold, the slow dynamics makes oscillation frequency highly sensitive to weak external forcing, so that even small maternal cues could effectively entrain a nascent clock. Distinguishing between these two mechanisms requires tracking both period and amplitude across development, which have not previously been available for any embryonic circadian tissue.

In this study, we pinpoint when circadian rhythms first emerge in the embryonic mouse brain. Using bioluminescent reporters for PER2 and *Bmal1*, we identify that the 4VCP is the earliest detectable clock, governed by SNIC-like bifurcation dynamics. We demonstrate that this onset mechanism renders the nascent clock highly sensitive to mid-gestational fluctuations in the maternal clock. Transcriptional profiling of mother and embryo throughout pregnancy reveals three distinct epochs in clock gene expression coinciding with 4VCP differentiation. Initially coupled to the mother, both maternal and embryonic clocks undergo transient destabilization, after which the embryo establishes autonomous circadian organization approaching canonical TTFL architecture. As the 4VCP matures, it ceases to entrain to external temperature cycles and transitions toward robust, self-sustained oscillation.

Results

The 4VCP exhibits autonomous circadian oscillations prior to the SCN

The embryonic SCN is widely recognized as the earliest reported brain region to exhibit a detectable circadian rhythm, emerging between E14.5 and E15.5 (Wreschnig et al., 2014; Carmona-Alcocer et al., 2018). To test whether this holds across the brain, we prepared brain slices from E15.5 PER2::LUC$^{+/-}$ embryos and performed bioluminescence imaging for 5-7 days (**Fig. 1A**-**C**, **Movie S1**). Spectral analysis revealed two consistent loci with ~24 h periods, circadian power exceeding 30% (see Materials and Methods), and high RMS amplitude (**Fig. 1Ca**,**1Cb**, **Fig. S4**). The ventral locus (white arrow) was RORA-positive, confirming its identity as the SCN (VanDunk et al., 2011), whereas the posterior structure (red arrow) was TTR-positive, a known marker for the CP (Kaiser and Bryja, 2020) (**Fig. 1Cc**). When analysis was restricted strictly to these regions, robust rhythms with periods between 20 and 28 h were detected, with circadian power of 59.4 ± 0.8% in the SCN and 40.4 ± 0.4% in the 4VCP (**Fig. 1Cd**). The pituitary gland also exhibited rhythmicity (46.9 ± 0.4%), but with lower RMS amplitude (10.2 ± 0.2 AU vs. SCN: 15.5 ± 0.9 AU, 4VCP: 15.5 ± 0.5 AU; both $p < 0.0001$) (**Fig. S4**).

At E13.5, no circadian oscillations were detected in ventral structures corresponding to SCN progenitors, consistent with previous reports (Wreschnig et al., 2014; Carmona-Alcocer et al., 2018) (**Fig. 1D**, **Movie S2**). However, the 4VCP (red arrow) exhibited a near-24 h rhythm with strong circadian power of 30.0 ± 0.7% (vs. hypothalamus: 20.7 ± 0.1%) and high RMS amplitude (**Fig. 1Db**, **Fig. S4**), which we confirmed after restricting the analysis to the 4VCP (**Fig. 1Dd**). At E11.5, no significant circadian rhythm was detected in whole brain slices (**Fig. 1E**, **Movie S3**). To confirm that this rhythm was endogenous, we dissected E13.5 4VCPs and recorded bioluminescence *ex vivo* (**Fig. 1F**, **Movie S4**). The isolated 4VCP explant exhibited robust

127 rhythmicity with circadian power of ~40%, well above the detection threshold determined from
128 blank luciferase medium (Blk, < 20%) (**Fig. 1Fb**).
129
130 **Tracking the precise timeline of 4VCP clock emergence**
131
132 To pinpoint the exact onset of clock emergence, we tracked PER2::LUC bioluminescence in
133 isolated 4VCPs from E9.5, when the CSF compartment first forms (Chau et al., 2015), through to
134 postnatal stages via LumiCycle, recording from 110 embryos (3-11 per stage, from at least 2-3
135 litters) for 5-7 days (**Fig. 2**). The oscillation period was initially long and highly dispersed at E9.5
136 (27.50 ± 2.12 h; $p < 0.0001$, $n = 3$ detectable oscillations), converging toward a stable 24 h by
137 E11.5 (24.98 ± 0.54 h; $p > 0.1$, $n = 11$). This marked the onset of detectable oscillations, as
138 circadian power exceeded 20% (31.42 ± 1.90% at E11.5, $p < 0.0001$, $n = 15$; vs. 18.01 ± 2.43%
139 at E10.5, $p > 0.05$, $n = 15$) (**Fig. 2A**,**C,D**). These early oscillations were weakly sustained with low
140 RMS amplitude. By E12.5, they persisted throughout recording, with amplitude increasing further
141 at E13.5. The rhythm became fully circadian at E15.5 (24.47 ± 0.60 h; $n = 5$), with high circadian
142 power (50.96 ± 3.42%; $n = 5$) approaching the 2-day window ceiling of ~60% (**Fig. 2A,C,D**).
143
144 To characterize the molecular assembly of this clock, we also measured from the *Bmal1-ELuc*
145 reporter strain. Interestingly, *Bmal1-ELuc* oscillations with a ~24 h period were only observed
146 from E13.5 to E14.5, approximately two days after the emergence of PER2 oscillations (**Fig.**
147 **2B,C,D**). Sigmoidal fits to circadian power trajectories estimated the exact emergence time (T_e)
148 (see Materials and Methods). PER2::LUC oscillations became circadian at E11.7 ± 0.1, whereas
149 *Bmal1-ELuc* oscillations emerged later at E13.5 ± 0.7 *ex vivo* (**Fig. 2D**). This delayed *Bmal1* aligns

150 with the sudden upward shift in PER2::LUC circadian power above 20% observed at E12.5-
151 E13.5 (**Fig. S5A**).
152
153 Because the circadian clock and developmental programs are deeply intertwined, we mapped
154 the embryonic 4VCP's developmental trajectory by quantifying progenitor markers (*Gli3*, *Ki67*,
155 *Wnt1*, *Nanog*) (Awatramani et al., 2003; Hunter and Dymecki, 2007) and differentiation markers
156 (*Aqp1*, *Otx2, Ttr*, *Wnt5a*) (Lun et al., 2015; Langford et al., 2020). Progenitor markers
157 predominated from E9.5 to E11.5, whereas differentiation genes dominated from E14.5 onward
158 (**Fig. 2E**). Sigmoidal fits estimated the progenitor half-minimum at E13.6 ± 0.8 and the
159 differentiation half-maximum at E13.5 ± 0.2, coinciding with *Bmal1-ELuc* emergence (T_e = E13.5
160 ± 0.7) (**Fig. 2G**). This defines three epochs: the undifferentiated state (E9.5-E12), the transition
161 state (E12-E15), and the differentiated state (E15-E16.5). Notably, PER2::LUC oscillations (T_e =
162 E11.7 ± 0.1) appear during the early transition, preceding both *Bmal1* rhythmicity and the
163 differentiation switch, an order that is atypical for a canonical TTFL where *Bmal1* drives *Per*
164 transcription (**Fig. 2G**).
165
166 Finally, we compared the emergence time of PER2::LUC rhythms across the brain and peripheral
167 organs in isolated explant culture. Among all tissues tested, the 4VCP was the first to become
168 circadian, preceding the lateral ventricle CP (LVCP: E12.4 ± 0.2), the SCN (E14.2 ± 0.4), and
169 peripheral organs such as the liver (E14.5 ± 0.6) and kidney (E15.1 ± 0.3) (**Fig. 2F**,**G**). In the SCN,
170 the period approached 24 h at E14.5 (24.47 ± 2.35 h, n = 7) and became fully circadian at E15.5
171 with high circadian power (44.56 ± 2.48%, n = 3).
172
173 **Abrupt, SNIC-like onset and synchronization of clock emergence**

The type of bifurcation underlying oscillation onset can be deduced by tracking how amplitude and period evolve over development. Circadian clocks have long been modelled as supercritical Hopf bifurcations, which behave analogously to resonance: amplitude grows smoothly while the period remains fixed. A SNIC bifurcation is fundamentally different and oscillations appear abruptly at full amplitude but with an initially long period that shortens toward ~24 h. SNIC oscillation also displays pronounced phase sensitivity to weak perturbations (Ermentrout, 1996). In single-cell PER2::LUC imaging, we observed a sharply defined clock onset with a stepwise amplitude increase (**Fig. 3A**) and an initially long period (**Fig. 3B**), hallmarks of a SNIC bifurcation. Information-theoretic model comparison favored a discrete amplitude step and period decay, consistent with SNIC dynamics rather than the gradual emergence expected from a Hopf bifurcation (**Fig. S5C**). This was further supported at the tissue level: whole-tissue luminometry confirmed a long initial period at E9.5 (26.4 ± 4.3 h), which converged to ~24 h by E17.5 (24.3 ± 1.1 h) (**Fig. 2C**), and period scatter plots fit the SNIC scaling law $1/\sqrt{(t - t_0)}$. While the whole-tissue luminometry amplitude increased linearly, this reflected growth in 4VCP cell number across development (**Fig. S5B**). *In vivo*, *Per2* transcript periods similarly reached ~28 h at E9.5 before converging toward 24 h (**Fig. S8**).

At the population level, we observed an abrupt rise in cellular synchronization between E13.5 and E14.5 (**Fig. 3C**, **Fig. S6A**) quantified by the Kuramoto order parameter (0 indicates the absence of synchronization; 1 denotes complete synchronization). This shift parallels the sudden synchronization onset reported in the SCN (Carmona-Alcocer et al., 2018). These changes demonstrate that the clock emergence process at both single-cell and population levels is not gradual ramp-up, but rather a discretely staged event occurring in specific developmental epochs.

199 **Temperature cycles drive embryonic 4VCP rhythmicity until E16.5**

200 Since systems near a SNIC bifurcation are highly sensitive to low-amplitude stimuli, we
201 hypothesized that subtle maternal circadian temperature cycles could serve as an early, non-
202 blood-borne driver of the nascent clock. During pregnancy, the amplitude of the maternal core
203 body temperature rhythm dampens to ~1 °C and further drops to ~0.5 °C by mid-gestation
204 (Smarr et al., 2016). This ~0.5 °C fluctuation is considered too small to entrain adult peripheral
205 clocks *in vitro* (~4 °C, Brown et al., 2002; ~2.5 °C, Buhr et al., 2010; ~1.5 °C, Abraham et al.,
206 2010).

207

208 To test this directly, we recorded PER2::LUC activity in cultured embryonic explants subjected
209 to temperature entrainment. Since maternal body temperature at E6 varies between 37.5 °C and
210 37 °C (Wharfe et al., 2016), we applied an initial temperature of 37 °C for 2 days, followed by 12
211 days of a 37-37.5 °C (Δ0.5 °C) square-wave cycle with a 26 h period (**Fig. 3D**). We evaluated
212 explants of the 4VCP and lung at E14, E16, and E18 and observed a clear, stage-dependent
213 transition in entrainability (**Fig. 3E**). At E14, the 4VCP PER2 rhythm phase-locked to the 26 h
214 temperature cycle (circular SD = 0.47 rad; n = 5). At E16, entrainment occurred only after an
215 initial transient (circular SD = 0.70 rad; n = 4). By E18, the 4VCP was resistant to entrainment,
216 failing to phase-lock to the 26 h cycle (circular SD = 1.16 rad; n = 4) (**Fig. 3F**). The lung entrained
217 at all stages, reflecting its prolonged maturation and weaker intercellular coupling (Abraham et
218 al., 2010) (**Fig. 3E,F**). The LVCP mirrored the 4VCP, losing entrainability by E18, whereas the
219 SCN remained entrainable at E18, consistent with its network immaturity at this stage (Bedont
220 and Blackshaw, 2015) (**Fig. S6B**, **Table S2**).

221

222 By E18, the 4VCP behaved as a robust, adult-like limit cycle oscillator, resistant to small
223 perturbations. Despite receiving higher-amplitude blood-borne signals from ~E16 onward, the
224 fully differentiated 4VCP effectively "closed" its window of extreme sensitivity to low-amplitude
225 ambient fluctuations to operate as an independent pacemaker.
226

227 **Transcriptional profiling reveals non-canonical early rhythms in three epochs**

228 We sampled embryonic 4VCPs from 127 PER2::LUC litters across E9-E16 at four circadian time
229 points (ZT2, ZT8, ZT14, ZT20) per embryonic day for RT-qPCR. The highest transcript levels
230 were those of *Clock, Rora,* and *Chrono*, rather than *Bmal1* and *Per1/2/3* as expected from adult
231 TTFL networks (**Fig. 4A**). Transcripts followed distinct developmental trajectories: some
232 increased gradually (*Clock, Dbp, Rev-Erbα/β, Bmal1*, *Per1*), others peaked sharply around E14.5
233 (*Rora, Chrono*, *Per2/3*), and a few remained relatively stable (*Rorc*, *Cry2*). The divergent
234 trajectories of *Bmal1* and *Per2* likely explain the onset-timing discrepancy between *Bmal1-ELuc*
235 and PER2::LUC reporters (**Fig. 2G**).
236

237 To characterize developmental evolution of the molecular rhythms, we quantified the circadian
238 power of each transcript using SST-CWT analysis (Materials and Methods; **Fig. S7A**, **S8**).
239 Hierarchical clustering of circadian power revealed five clusters with unique onset patterns (**Fig.**
240 **4B**): *Clock* (Cluster 1) becomes highly circadian from E9.5; *Per3*/*Cry2* (Cluster 2) are circadian
241 early on (E9.5-E10.5) with a maximum power of ~40-50%; *Rorc*/*Per1* (Cluster 3) emerge as
242 circadian later, around E13.5; *Rora*/*Rev-Erbα*/*Per2*/*Chrono*/*Bmal1* (Cluster 4) show early
243 rhythmicity from E9.5 (except for *Bmal1*) but lose it during the E12-E15 epoch; *Dbp*/*Rev-Erbβ*
244 (Cluster 5) lack circadian rhythmicity across all measured stages. Several clock genes thus
245 oscillate around E10.5, well before structural differentiation. Surprisingly, these empirical clusters

246 do not align with the promoter-motif architecture expected from canonical TTFL logic (Ukai-
247 Tadenuma et al., 2008), nor with the normalized density of transcription factor binding motifs
248 quantified near their transcription start site (**Fig. S7B**). For instance, *Per1* and *Per2* both contain
249 glucocorticoid and cAMP response elements (GREs and CREs) that can reset the CP clock (Liška
250 et al., 2021), yet they fall into completely different onset clusters. This suggests that early
251 embryonic circadian gene expression dynamics in the 4VCP cannot be solely explained by the
252 transcriptional logic of the TTFL.
253
254 Spectral analysis across stages revealed unstable periods, visible as broad smears for most
255 genes between E12 and E15 (**Fig. 4C**, **Fig. S7A**,**S8**), contrasting with the stable *Bmal1* period in
256 maternal 4VCP (**Fig. 5B**, **Fig. S10A**). To quantify this globally, we calculated normalized spectral
257 entropy, where high values indicate power dispersed across frequencies. Mean entropy peaked
258 between E12.3 and E15.3, confirming a significant transition epoch (permutation clustering, $p <$
259 0.05; **Fig. 4C**).
260
261 To investigate the functional consequences of this early clock, we tracked the expression of
262 clock-controlled genes (CCGs) encoding tight junctions (*Cldn1/2/3/11*, *Ocln*) known to be
263 present in both adult and embryonic CP epithelium (Wolburg et al., 2001; Steinemann et al.,
264 2016). Functional E-boxes have been identified in several tight junction genes (Mei et al., 2015;
265 Oh-oka et al., 2014), and we confirmed the robust expression of these transcripts in the
266 embryonic 4VCP from E9.5 onwards (**Fig. S9A**). Consistent with this, *Cldn1* and *Cldn3* showed
267 strong temporal correlations with *Per1* and *Rev-Erbβ* expression, respectively (**Fig. S9C**).
268 However, their circadian power varied across epochs: *Cldn1* was circadian from ~E12.5, *Cldn3*
269 from E10.5 to E14.5, and others (*Cldn2/11*, *Ocln*) did not exhibit strong rhythms until E15.5 (**Fig.**
270 **4F**, **Fig. S9D**). Similar to the core clock genes, the developmental timeline of circadian power in

271 tight junction transcripts clustered independently of their promoter motifs (e.g., *Cldn1/3* and *Ocln*
272 did not cluster together despite the presence of validated E-boxes) (**Fig. 4E, Fig. S9B**). If these
273 transcripts translate to rhythmic protein levels, it would imply that the 4VCP can functionally gate
274 the blood-CSF barrier circadianly as early as ~E12.5, with CLDN3 acting as the first circadian
275 gatekeeper, later relayed by CLDN1. Tight junction-mediated paracellular transport is a key
276 pathway through which the blood-CSF barrier regulates the CSF (Ghersi-Egea et al., 2018).
277
278 Gene expression phases from E9 to E16 revealed a progressive maturation of the molecular
279 circuit (**Fig. 4G**): phases were broadly distributed at E10.5, shifted dramatically into the
280 complementary 12-h window by E14.5, and underwent strict bipartite polarization by E16.5, with
281 *Clock*, *Chrono*, and *Cry2* antiphasic to the main group. This organization approaches the
282 canonical TTFL phase organization but remains immature, as *Bmal1* is still in-phase with the E-
283 box-driven group.
284
285 These patterns confirm three epochs of clock development: the undifferentiated epoch (E9.5-
286 E12), with weak, non-canonical oscillations; the transition epoch (E12-E15), with period instability
287 and phase reorganization; and the differentiated epoch (E15 onward), with stable, highly
288 circadian oscillators approaching the phase organization of the mature TTFL.
289
290 **Maternal clock instability and feto-maternal reorganization**

291 The absence of sustained *Bmal1-ELuc* rhythms in the embryonic 4VCP between E10.5 and E12.5
292 *ex vivo* (**Fig. 2B**), despite clear day-night variation *in vivo* over the same interval (**Fig. S8**),
293 suggests that early circadian gene expression depends on maternal cues (Wong et al., 2022).
294 Yet direct systemic maternal influence via the bloodstream is absent at this early stage. We

295 performed spectral profiling of clock gene expression in the 4VCP of 102 wild-type dams (**Fig.**
296 **S10A**). While all genes exhibited circadian rhythmicity at the transcript level (**Fig. 5A,B**; **Fig.**
297 **S10A**), the circadian power, period, and phase of *Per2*, *Rora*, and *Rorc* decreased or fluctuated
298 significantly as pregnancy progressed (**Fig. 5B,C**).
299
300 Comparison with non-pregnant controls revealed that pregnancy drastically altered both the
301 amplitude and phase of clock transcripts, with the most profound shift at G12.5-G13.5,
302 producing a distinct phase organization in the maternal 4VCP (**Fig. 5D**, **Fig. S10B,C**). Behavioral
303 monitoring of free-running locomotor activity confirmed a significant drop in circadian power
304 during pregnancy (*$p < 0.05$; two-sample *t*-test; **Fig. 5E,F**) consistent with reported declines in
305 wheel-running during gestation (Yaw et al., 2021). In cases of presumed resorption, robust
306 circadian rhythmicity was restored rapidly, accompanied by the return of the estrous cycle
307 rhythm (**Fig. 5E**). These data demonstrate that the maternal circadian rhythm is transiently
308 disrupted during pregnancy at both molecular and behavioral levels.
309
310 Pairwise correlations between dam and embryo clock gene expression revealed a global loss of
311 maternal-fetal correlation at E12.5, contrasting with highly organized patterns at E16.5 (**Fig. 5G**,
312 **Fig. S11A**,**B**). Maternal-embryonic coupling undergoes a transient destabilization around E12-
313 E13 before re-establishing tighter correlation patterns after E14. Dual-radius phase plots
314 revealed that correlation shifts were rarely one-sided (with *Bmal1* as a notable exception) (**Fig.**
315 **5H**), and the shift in maternal *Per2* phase coincided precisely with the reorganization of coupling
316 patterns (**Fig. S11C**,**D**).
317

318 Finally, since both 4VCP clocks are destabilized during mid-pregnancy, we examined whether
319 their physical interface, the placenta, was similarly affected. As the placenta matures, embryonic
320 nutrient supply shifts from histiotrophic (yolk sac-based) to hemotrophic (blood-based),
321 beginning around E10 and becoming fully functional by E12.5-E13.5 (Elmore et al., 2022). We
322 separated embryonic and maternal placental tissues and recorded PER2::LUC and *Bmal1-ELuc*
323 bioluminescence *ex vivo* from E9.5 to E20.5. The embryonic placenta lacked autonomous
324 circadian oscillations (Čečmanová et al., 2019) (**Fig. S12A**), whereas the maternal placenta
325 exhibited robust rhythms that underwent transient attenuation during mid-gestation (E13-E15)
326 (**Fig. S12B**). Inverted Gaussian fits estimated a mid-gestational nadir in circadian power for
327 PER2::LUC and *Bmal1-ELuc* at ~20-30%, centered at E15.3 ± 0.4 and E15.6 ± 0.6, respectively.
328 This circadian dip aligns closely with the functional maturation of the hemotrophic interface
329 (Elmore et al., 2022).
330
331 Taken together, these results demonstrate that coupling between maternal and embryonic
332 clocks is highly dynamic, undergoing shared transient disorganization around E13.5 before the
333 embryonic system consolidates its circadian architecture.
334

335 **Discussion**

336
337 Our study identifies the embryonic CP as the earliest detectable brain circadian clock, emerging
338 ~2.5 days before the SCN. We observed a staged assembly of the transcriptional clock circuit
339 that coincides with cellular differentiation. The emergent rhythm exhibits hallmarks of a SNIC
340 bifurcation, rendering the nascent clock highly sensitive to low-amplitude stimuli such as
341 maternal core body temperature. Circadian profiling across embryonic development revealed

342 three epochs characterizing *in vivo* clock emergence that closely track the differentiation
343 program of the 4VCP. Strikingly, the middle transition epoch exhibits a transient destabilization
344 of both maternal and embryonic 4VCP clocks (**Fig. S13**).
345
346 Contrary to the prevailing assumption that the SCN is the first circadian structure in the
347 mammalian embryo, our data show that the 4VCP clock emerges significantly earlier. While our
348 survey was limited to selected sagittal sections rather than the full three-dimensional extent of
349 the brain, the 4VCP was consistently the earliest structure to display autonomous circadian
350 rhythmicity. Of note, the first three structures identified as circadian by E15.5, the CP, SCN, and
351 pituitary gland, are positioned to regulate brain homeostasis and endocrine signaling, and they
352 maintain strong oscillations postnatally (Myung et al., 2018).
353
354 As the first clock in the embryonic brain, the 4VCP carries profound functional implications.
355 Because the adult CP is a robust oscillator capable of entraining the SCN both *ex vivo* and *in*
356 *vivo* (Myung et al., 2018), the early 4VCP clock could similarly influence the subsequent
357 emergence of the SCN clock. Furthermore, as a secretory tissue, a circadian CP could
358 rhythmically regulate CSF volume and composition, periodically releasing morphogens and
359 growth factors (Kaiser and Bryja, 2020; Saunders et al., 2023; Lun et al., 2015). The
360 neuroepithelium lining the ventricles would thereby receive temporally patterned cues capable
361 of modulating transcription factor expression in neural progenitors and influencing cell fate
362 decisions (Lamus et al., 2020; Lehtinen et al., 2011; Subashini et al., 2017). For example,
363 oscillations of basic-helix-loop-helix (bHLH) factors (e.g., *Hes1*, *Ascl1*, *Olig2*) promote cell
364 proliferation, whereas sustained expression drives differentiation (Imayoshi et al., 2013). By
365 temporally gating differentiation, the progenitor pool can expand sufficiently before neurogenesis

366 begins, a prerequisite for establishing the correct number of neurons and neural progenitors in
367 the adult brain (Caviness et al., 1995; Kriegstein and Alvarez-Buylla, 2009).
368
369 Studying the embryonic 4VCP clock both *in vivo* (with maternal entrainment) and *ex vivo*
370 (isolated) allowed us to map the relationship between clock assembly and the tissue
371 differentiation program through three epochs. During the initial undifferentiated stage (E9.5-
372 E11.5), despite a progenitor profile dominated by markers such as *Gli3* and *Ki67* (**Fig. 2E**), we
373 observed early circadian expression of select clock genes (*Per2/3, Rora, Clock, Chrono*) *in vivo*
374 (**Fig. S8**). This contrasts with *in vitro* studies showing that induced pluripotent stem cells (iPSCs),
375 embryonic stem cells (ESCs), and other pluripotent stem cells (PSCs) lack circadian clocks
376 (Yagita et al., 2010; Kowalska et al., 2010; Kaneko et al., 2023). This discrepancy likely arises
377 because the *in vivo* embryonic 4VCP is exposed to maternally driven signals. Since the embryo
378 lacks a direct blood connection to the dam at this stage, these signals must be ambient and low
379 in amplitude. We demonstrated that the periodicity of maternal body temperature provides one
380 such environmental cycle within the uterus, capable of driving the 4VCP clock until E16.5.
381 Because this early ambient driving is restricted to highly responsive tissues such as the 4VCP, it
382 underscores the importance of evaluating clock rhythmicity in a tissue-specific manner. Whole-
383 embryo analyses, which dilute these localized rhythmic signals with non-rhythmic bulk, have
384 previously missed these early clocks (Cao et al., 2022; Dolatshad et al., 2010).
385
386 During the transition phase (E12-E15), cellular differentiation is a prerequisite for full clock
387 autonomy (Yagita, 2024; Yagita et al., 2010; Kowalska et al., 2010; Kaneko et al., 2023; Umemura
388 et al., 2017). However, we note that *ex vivo*, the rhythm of the canonical activator *Bmal1* appears
389 much later than that of *Per2*, suggesting that this embryonic clock is not initially established by
390 classic BMAL1:CLOCK-driven feedback. *In vivo*, as differentiation begins, the embryonic rhythm

391 is notably weakened, although transcripts like *Clock*, *Cry2*, and *Cldn3* remain circadian. This
392 unstable epoch is mirrored in the maternal 4VCP and placenta, where we observed a significant
393 decrease in PER2::LUC and *Bmal1-ELuc* circadian power, but not in maternal peripheral organs
394 like the liver (Canaple et al., 2018). The mid-gestational instability coincides with increased
395 activity of 11β-hydroxysteroid dehydrogenase type 2 (11β-HSD2; E12.5-E16.5), which
396 inactivates glucocorticoids (Salvante et al., 2017). As the placenta matures, this selective
397 endocrine gating likely attenuates maternal influence (Astiz and Oster, 2021), creating a shielded
398 developmental window for the embryonic clock to undergo autonomous self-organization.
399
400 The discrepancy between our *in vivo* and *ex vivo Per2* data during this epoch warrants careful
401 interpretation. One possibility, proposed by others (Yagita, 2024), is that the loss of circadian
402 rhythmicity in many transcripts around E12-E15 reflects active suppression of the embryonic
403 clock to permit differentiation. Since the 4VCP clock is autonomous *ex vivo* by E12.5, fluctuating
404 maternal signals, which are themselves unstable during this window, could exert this inhibitory
405 effect on the embryonic clock. An alternative interpretation is that the period instability during
406 the transition epoch (E12-E14.5) reflects a transient state of low intra-tissue synchrony rather
407 than active suppression. Before E12, nascent 4VCP oscillators near the SNIC threshold possess
408 intrinsically variable periods but are frequency-locked by maternal temperature cycles. Around
409 E12-E13, the maternal clock destabilizes. Compounded by progressive placental shielding, the
410 maternal drive withdraws before endogenous intercellular coupling has matured, even as the
411 underlying cellular bifurcation dynamics shifts toward a Hopf regime during TTFL maturation.
412 Consequently, the tissue-level readout averages over desynchronized cells, effectively blunting
413 any underlying rhythms. By E14.5, intrinsic coupling rises abruptly, and individual cellular
414 rhythms become coherently detectable in whole-tissue *in vivo* quantification. Beyond the effects
415 of entrainment or synchrony, the apparent delay in *Per2* rhythmicity may simply reflect the

416 different biomolecules being measured. At E11.7, PER2 protein oscillates with a ~24 h period *ex*
417 *vivo*, whereas *Per2* transcripts do not yet cycle *in vivo*. This discrepancy is expected, as robustly
418 cycling proteins frequently originate from non-cycling transcripts through post-transcriptional
419 regulation (Qian et al., 2023; Robles et al., 2014; Mauvoisin et al., 2014). Conversely, BMAL1
420 protein can be post-translationally modified to remain functionally inactive, potentially preventing
421 premature interference with ongoing developmental programs (Umemura et al., 2022). This
422 illustrates why transcript presence does not always equate to functional integration into the TTFL
423 circuit.
424
425 Following this transient destabilization, the fully differentiated 4VCP (E15-E16.5) exhibits a more
426 robust, autonomous clock *ex vivo*. *In vivo*, the majority of embryonic clock genes regain circadian
427 rhythmicity and organize their phases into two antiphasic groups, with *Clock* adopting the
428 opposing phase. This restoration likely reflects the combined influence of SCN emergence,
429 strengthened intercellular synchrony, and the intrinsic capacity of *Bmal1* to oscillate. In the dam,
430 although the 4VCP clock appears restored, the free-running behavioral rhythm remains impaired,
431 potentially reflecting continued instability in the SCN. By contrast, in the 4VCP, both maternal
432 and embryonic genes align in phase during this epoch, suggesting a synchronized maternal-fetal
433 relationship. However, our study design does not allow us to determine the directionality of
434 maternal-embryonic coupling.
435
436 Multiple lines of evidence indicate a relatively autonomous embryonic clock by late gestation. In
437 mice, maternal influence on pup behavioral synchrony occurs early rather than late in gestation
438 (Davis and Gorski, 1988; Jud and Albrecht, 2006), and in humans, preterm infants display
439 detectable circadian-like rhythms in body temperature, heart rate, and rest-activity in the NICU
440 (Bueno and Menna-Barreto, 2016; Govindan et al., 2024), with 24 h sleep-wake rhythms

441 appearing earlier in preterm than in full-term infants (Guyer et al., 2015). Our data show that the
442 4VCP remains sensitive to 0.5 °C temperature cycles at E16 but not E18, consistent with
443 entrainment observed in late embryos following maternal restricted feeding (Canaple et al.,
444 2018).
445
446 The early emergence of the circadian clock in the 4VCP at E11.5-E12.5 challenges the long-held
447 view of the SCN as the origin of circadian pacemaking in the mammalian brain and, by extension,
448 the presumed locus of developmental onset. Our findings further reveal that the clock emergence
449 in the CP is a discrete, non-canonical developmental process, with rhythmic expression of *Rora*,
450 *Per2/3*, and *Chrono* detectable as early as E9.5. Furthermore, while mature circadian oscillators
451 are classically modelled by Hopf bifurcations, this early developmental transition is governed by
452 highly sensitive SNIC bifurcation dynamics. The multi-stage assembly and sudden external
453 emergence of the clock strongly support the paradigm that circadian clock onset is a
454 programmed developmental event. By characterizing the precise timing, locus, and mechanism
455 of the brain's first clock, this work provides a new framework for understanding maternal-fetal
456 interactions and insights into early circadian homeostasis with direct relevance to preterm and
457 neonatal care.
458

459 **Material and Methods**

460

461 **Mice**

462 Homozygous PER2::LUC mice (B6.129S6-*Per2*^{tm1Jt}/J, RRID: IMSR_JAX:006852) and
463 heterozygous *Bmal1-ELuc* mice (Nakajima et al., 2010; a gift from Daisuke Ono, Nagoya
464 University), maintained on the C57BL/6J background, were crossed with wild-type C57BL/6J

465 animals to generate heterozygous PER2::LUC$^{+/-}$ or *Bmal1-ELuc*$^{+/-}$ embryos. Mice were
466 maintained under equinox light-dark (LD) cycles (12h light:12h dark; lights on at 07:00, off at
467 19:00), with schedules controlled by LocoBox software (Truong and Myung, 2023). Ambient
468 temperature and humidity were maintained at 24.0 ± 1.8 °C; 50.2 ± 8.7% RH. Zeitgeber Time
469 (ZT) 0 was defined as the time of lights-on. For tissue sampling at ZT14 and ZT20, a reversed
470 dark-light (DL) cycle was used (lights on at 22:00, off at 10:00) (**Fig. S1A**). We validated that
471 embryonic gene expression levels under the reversed cycle matched those under standard LD
472 cycles at E13.5 (**Fig. S1B**). All animal protocols were approved by the Institutional Animal Care
473 and Use Committee (IACUC) of the Taipei Medical University Laboratory Animal Center
474 (protocols LAC-2019-0430, LAC2022-0381, LAC2022-0477, LAC2023-0037, and LAC2023-
475 0038).
476
477 **Circadian actimetry**

478 Female wild-type C57BL/6J mice (6 weeks old) were housed in constant darkness (DD) for two
479 weeks to get their baseline activity, followed by one week under a 12:12 LD cycle to synchronize
480 their phase with the LD-housed males. Following a single night of mating, females were isolated,
481 weighed, and returned to DD for ~21 days. Locomotor activity was continuously recorded using
482 LocoBox (Truong and Myung, 2023). Pregnancy was confirmed by weighing females at G8.5
483 and/or G13.5 under DD, and activity monitoring continued until parturition. Cage changes were
484 restricted to G8.5 or G13.5 to minimize disruptions to locomotor recordings.
485
486 **Tissue isolation and explant culture**

487 ***Direct dissection.*** Tissue culture and bioluminescence recording were performed according to
488 our previous protocols (Myung et al., 2018). Pregnant female mice were anesthetized with

489 isoflurane and euthanized at defined ZTs. Brains and embryos were rapidly extracted into ice-
490 cold Hank's balanced salt solution (HBSS; Sigma-Aldrich) supplemented with penicillin-
491 streptomycin (10,000 U/mL; Gibco) and HEPES (1 M, pH 7.4). Embryonic tissues were dissected
492 under a stereomicroscope after decapitation. For E9.5, the prosencephalon (containing SCN and
493 LVCP progenitors) and rhombencephalon (containing 4VCP progenitors) were collected. For
494 E10.5-E12.5, the 4VCP was extracted from the inferior part of the hindbrain roof plate epithelium
495 (lower rhombic lip, rhombomere 2-8), located between the otic vesicles and the posterior part of
496 rhombomere 1 (Hunter and Dymecki, 2007). The cortical midline served as the anatomical
497 landmark for LVCP progenitors. After E12.5, the CP dissection was similar to that of the adult.
498 The precision of 4VCP isolation throughout development was validated by RT-qPCR (**Fig. S2**).
499 SCN progenitors from E10.5 to E13.5 were dissected from the ventral hypothalamus between
500 the optic cups. After E13.5, the SCN and the optic chiasm were clearly distinguishable, and
501 dissection was performed as in the adult. This protocol was also used to isolate maternal and
502 embryonic tissues in ice-cold PBS for biomolecular experiments.
503
504 ***Placenta dissection.*** The maternal decidua (light pink outer layer, representing maternal
505 placenta) was mechanically separated from the junctional zone and labyrinth (darker pink inner
506 layer, representing the embryonic placenta). The loose junction between these two layers
507 allowed dissection with forceps (Čečmanová et al., 2019).
508
509 ***Tissue slicing and explant culture.*** Embryonic heads or brains (E11.5, E13.5, E15.5) were
510 briefly submerged in two successive baths of low-melting-point agarose (2% w/v; CAS 9012-
511 36-6) at 37 °C, embedded in an agarose block, and sliced in ice-cold HBSS using a vibratome
512 (VT1000S, Leica Biosystems). Slices (300 μm thick) were cut using a diamond blade (Delaware
513 Diamond Knives) advancing at ~0.025 mm/s. Explants were cultured on culture membrane

514 inserts (PICM0RG50, Merck Millipore) in 35-mm dishes containing 1 mL DMEM (Sigma-Aldrich)
515 supplemented with B-27 (Gibco) and 200 μM beetle luciferin (Promega). Dishes were sealed with
516 high-vacuum grease (Molykote, DuPont) and maintained at a strictly controlled 37.00 ± 0.01 °C
517 in a hybrid refrigerator-heater incubator (MIR-154-PA, PHCbi), monitored closely by placing an
518 iButton (DS1921L, Maxim Integrated) adjacent to the dishes.
519

520 **iDISCO tissue clearing and immunofluorescence labeling**

521 Post-culture brain slices were cleared using the standard iDISCO protocol
522 (https://idisco.info/idisco-protocol). Slices were fixed in 4% PFA, washed in PBS for 3 days,
523 dehydrated in a MeOH/H_2O series, and incubated overnight in 66% DCM/33% MeOH. Tissues
524 were bleached in 5% H_2O_2 overnight and rehydrated. Immunolabeling was performed at 37 °C,
525 beginning with permeabilization (1 day) and blocking (1 day), followed by primary antibody
526 incubation against TTR (chicken, 1:500, Genetex GTX85112; AB_10723946) for 2 days. Slices
527 were washed and incubated with a secondary antibody (anti-chicken Alexa Fluor 568, 1:500,
528 Abcam ab175477; AB_3076392) for 2 days. Following subsequent washing and blocking, slices
529 were incubated with a conjugated RORA antibody (1:500, Bioss BS-17164R-A350). Slices were
530 then transferred back to the micro glass vials to undergo final clearing, beginning with
531 dehydration in MeOH/H_2O followed by a 3h incubation in 66% DCM/33% MeOH at room
532 temperature. Finally, two 15-min incubations in 100% DCM were performed before mounting
533 the slices in dibenzyl ether under sealed coverslips, and imaged using a DM IL fluorescence
534 microscope (Leica Microsystems).
535

536 **Time-lapse bioluminescence luminometry and imaging**

537 ***Whole-tissue luminometry.*** PER2::LUC fusion protein reporters tracked PER2 abundance
538 through bioluminescence (RRID: IMSR_JAX:006852), while *Bmal1-ELuc* reporters tracked *Bmal1*
539 transcriptional activity (Nakajima et al., 2010). The overall bioluminescence from each tissue was
540 recorded every 15 min (108 s integration time per dish) using LumiCycle 32 (Actimetrics) with
541 four photomultiplier tubes (PMTs), housed in a refrigerator-heater incubator for precise
542 temperature control (MIR-154-PA, PHCbi). Temperature was recorded continuously throughout
543 the experiment.
544
545 ***Single-cell imaging.*** Imaging was conducted on a custom incubator-microscope system
546 equipped with a cooled-CCD camera (Orca R2, Hamamatsu) with water cooling, combined with
547 a 4x objective (NA 0.16, UPLXAPO, Olympus) coupled to a 0.35x reduction lens (U-TV0.35XC-
548 2, Olympus), and a stage-top incubator (INUG2-WELS, Tokai Hit). Images were acquired hourly
549 (60 min exposure time) with 4×4 binning using Micro-Manager 1.4 (Vale Lab, UCSF) via the
550 DCAM-API (Hamamatsu) driver.
551
552 **Real-time quantitative PCR (RT-qPCR)**

553 ***RNA Isolation, cDNA synthesis, and RT-qPCR.*** Embryonic or maternal 4VCPs collected at
554 ZT2, ZT8, ZT14, and ZT20 were pooled by litter (3-11 embryos/litter, minimum 2-3 litters per time
555 point). Total RNA isolation and RT-qPCR followed our previous protocol (Myung et al., 2018).
556 300 μL of TRK lysis buffer containing 2% β-mercaptoethanol was added to each sample,
557 followed by an equal volume of chloroform after intensive homogenization. After phase
558 separation and ethanol addition, microcolumns from the ENZA MicroElute Total RNA Kit (Omega
559 Bio-Tek) were used to collect total RNA, with a final elution volume of 21 μL in DEPC-treated
560 water. After evaluating the RNA concentration, cDNA was synthesized from 0.5-1 μg of total RNA

561 using SuperScript IV Reverse Transcriptase (Thermo Fisher Scientific) with oligo$(dT)_{20}$ primers.
562 PowerUp SYBR Green Master Mix (Applied Biosystems) was added to the cDNA samples, and
563 RT-qPCR was performed in technical triplicate on a QuantStudio 3 Real-Time PCR System
564 (Thermo Fisher Scientific). Primer sequences are detailed in **Table S1**.
565
566 ***Normalization.*** *Gapdh*, *Actb* (*β-actin*), and *Rpl13a* served as internal controls for embryonic
567 samples (Hildyard et al., 2022). G*apdh* and *Actb* were used for maternal samples. After outlier
568 exclusion (ROUT test, Q = 1%), the relative mRNA abundance for a given embryonic stage (n >
569 8) was calculated by normalizing to the maximum abundance observed between E9.5 and E16.5.
570 For example, at E9.5:

$$RNA_{\mathrm{E9.5}}\ (\%) = \frac{\mathrm{mean}\ (RNA_{\mathrm{E9.5}})}{\max\ (RNA_{\mathrm{E9.5-E16.5}})} \times 100 \qquad (1)$$

571

572 **Spectral analysis of bioluminescent time series and time of emergence quantification**

573 ***Preprocessing.*** Visualization and preprocessing of bioluminescence oscillations, including
574 periodogram and fast Fourier transform (FFT)-based spectral analysis, were performed on
575 Mathematica 13 (Wolfram Research) using the custom PMTAnalysis package
576 (http://sourceforge.net/projects/imaginganalysis). The first 6 h of all recordings were truncated
577 to remove handling transients. Circadian periods were estimated using FFT, and amplitudes
578 were quantified as the root mean square (RMS) of detrended oscillations over fixed windows (7
579 days for luminometry/4VCP imaging; 4 days for whole-brain slice imaging). For image analysis
580 of brain slices or the 4VCP, a 2×2-pixel grid was applied to the timelapse images after removal
581 of outlier pixels, and each ROI's standard deviation, center of mass, and mean grey value were
582 measured using ImageJ (NIH).

Circadian power. Using a sliding-window FFT (2-day for luminometry, 3-day for imaging), evolution of spectral power was tracked and visualized as spectrograms over time. Circadian power for each time window was calculated by integrating the spectral power within the circadian band (24 ± 4 h) relative to the full period range (3-58 h) (**Fig. S3**). This generated a time series reflecting the robustness of the circadian rhythm that accounts for damping, period variability, and noise. In addition, the overall circadian power was computed as the average of these window-wise circadian power values across the entire recording. For a perfect sinusoid in a 2-day window, the maximal circadian power reached ~60%, whereas for transient, rapidly damped oscillations, it fell below 20% (**Fig. S3**). The blank control (luciferase medium without tissue explant) showed a maximal circadian power of ~20% (*n* = 10) (**Fig. 2D**). For SCN and 4VCP explants, the half-maximal level of the fitted circadian power curve across development was ~30% (30.83 ± 2.36% and 31.28 ± 1.70%, respectively).

Emergence Time (T_e). Nonlinear curve fitting using a sigmoid function was applied to rigorously identify the onset of PER2::LUC and *Bmal1-ELuc* circadian rhythms. Blank recordings were used to estimate baseline circadian power and to provide null data points prior to E9.5. $\boldsymbol{T_e}$ was defined as the time point at which one-half of the maximum circadian power was reached:

$$P(t) = \frac{A}{1 + e^{-(t-T_e)/\tau}} + C_0 \qquad (2)$$

where $P(t)$ is the circadian power at time t (time of sampling for explant), A is the amplitude above baseline, τ is the time constant, and C_0 is the baseline determined from blank recordings.

Circadian promoter motif analysis

605 We analyzed promoter-proximal regions (-3 kb to +2 kb relative to TSS in GRCm39) of 12 core
606 circadian genes from our qPCR panel (**Table S1**). Gene coordinates and strand orientation were
607 retrieved from Ensembl via the REST API (https://rest.ensembl.org/). To ensure all windows were
608 extracted in the transcriptional orientation, minus-strand loci were reverse-complemented, so
609 that upstream and downstream were always defined relative to the direction of transcription. We
610 scanned these sequences for known transcription factor binding motifs relevant to circadian
611 regulation, including canonical and variant E-boxes (CACGTG, CACGTT, CACGTA), D-boxes
612 (TTATGAA, TTATGTA), REV-ERB/ROR response elements (RRE/RORE) (AGGTCA, GGGTCA,
613 [A/U]GGTCA), glucocorticoid response elements (GREs) including canonical palindromic
614 (AGAACA[ACGT]TGTTCT), *Per2*-specific variants ([AG]G[ACGT]TGT[TC]CT), as well as half-sites
615 ([AG]G[TA]ACA, TGT[TC]CT), and cAMP response element (CRE) half-sites (CGTCA, TGACG).
616 Motifs were represented either as exact sequences or regular expressions to capture degenerate
617 variants. Both forward and reverse-complement strands were scanned. Motif hits were identified
618 using regular expression search with overlapping match lookahead, followed by a priority-based
619 deduplication scheme favoring full palindromes and canonical motifs over partial or variant sites.
620 Motif density was expressed as the number of motifs per kilobase of sequence for each gene
621 and region. These densities are visualized as normalized motif densities (**Fig. S7B, S9B**).
622

623 **Hierarchical clustering and spectral analysis of gene expression profiles**

624 ***Hierarchical clustering.*** Expression levels were normalized using the internal control genes and
625 standardized using Z-scores. Pairwise distances were calculated using the Pearson correlation
626 r_{ij} as the distance metric between expression of genes i and j, and hierarchical clustering was
627 implemented via the seaborn.clustermap function (v0.11.2) in Python (v3.6.13). Clustering was
628 performed using average linkage, and results were visualized as a cluster heatmap with a

629 dendrogram that represents the similarity relationships. Average linkage distance $D(A,B)$ was
630 calculated as:

$$D(A,B) = \frac{1}{m \cdot n} \sum_{i \in A} \sum_{j \in B} d(i,j) \quad (3)$$

631 where m and n are the numbers of genes in clusters A and B, and $d(i,j)$ is the distance (1-r_{ij})
632 between genes i and j. We identified representative genes for each cluster by cluster centroids
633 calculated by averaging the Z-scored profiles of all member genes across time points. The gene
634 with the highest Pearson correlation to the centroid was designated as the representative, as it
635 best reflected the average temporal pattern of its cluster.
636
637 ***Synchrosqueezed continuous wavelet transform (SST-CWT).*** To analyze sparsely sampled,
638 non-stationary embryonic gene profiles, we applied SST-CWT to sharpen time-frequency
639 estimates, which reassigns CWT coefficients from a range of supporting frequencies to a more
640 precise instantaneous frequency (Daubechies et al., 2011). We implemented it using the Python
641 cwt_sst function from the ssqueezepy library (v0.6.5;
642 https://github.com/OverLordGoldDragon/ssqueezepy). Normalized gene expression time series
643 were detrended, mirrored, and extended prior to transform using a Morlet wavelet (90 voices per
644 octave). Although SST-CWT yields an amplitude spectrum, we refer to it here as a "power
645 spectrum" (the true power is the squared amplitude). Circadian power was calculated identically
646 to the bioluminescence data (24 ± 4 h band relative to the 3-58 h full range).
647
648 ***Phase dynamics and visualization.*** We estimated instantaneous phase (radians) along ridges
649 of the time-frequency representation. Instead of plotting phase alone, we generated phase-
650 weighted spectrograms, which multiply SST-CWT amplitude by its corresponding phase angle

651 to highlight dominant oscillatory components with phase context. To improve visual clarity,
652 colormap normalization and adaptive contrast scaling were applied using the maximum absolute
653 value of each map. An illustration of this approach using simulated data is shown in **Fig. S7A**.
654
655 ***Circular phase plots.*** To track phase across development (E10.5, E12.5, E14.5, E16.5), we
656 constructed circular phase plots based on the estimated instantaneous phase within the
657 circadian range (20-28 h). For each embryonic cluster, the representative gene was plotted
658 clockwise in a phase plot resembling a conventional clock, with 0 rad positioned at 12 o'clock.
659 Nonrepresentative genes from the same cluster were plotted with smaller, semi-transparent
660 markers for comparison. The left semicircle was shaded to distinguish early vs late phases.
661 Marker shape and color indicated cluster identity, and genes with circadian power ≥ 20% were
662 outlined in black. To assess potential maternal-embryonic coordination, dual-radius phase plots
663 were used: the inner ring showed embryonic cluster representatives, and the outer ring showed
664 selected maternal genes. Maternal-embryonic pairs were connected with dotted lines when both
665 exhibited circadian power ≥ 20% and their phase difference was $< \pi/2$ rad (≤ 6 h), indicating
666 possible phase alignment.
667
668 ***Sliding-window correlation.*** To assess temporal coordination among maternal and embryonic
669 genes, time series were padded by duplicating the first and last two points, and 5-timepoint
670 sliding windows were applied. Pearson correlation matrices were computed for each window,
671 generating a time-resolved sequence of correlations. Examples of dynamic correlation are
672 shown in **Fig. S11A**.
673

674 ***Normalized spectral entropy and identification of transition epoch.*** To quantify the
675 periodicity complexity in each detrended bioluminescence trace, we calculated the spectral
676 entropy from the SST-CWT of each gene's time series as:

$$H(t) = -\sum_{i} P_i(t) \frac{\log P_i(t)}{\log N} \tag{4}$$

677 where $P_i(t)$ is the normalized power in the i-th frequency bin at time t, and N is the number of
678 frequency bins. Low entropy corresponds to power concentrated in a single frequency, while
679 high entropy indicates power dispersed across multiple frequencies. To define the transition
680 epoch without relying on an arbitrary threshold, we employed a permutation clustering approach
681 on the pooled embryonic clock gene entropy trajectories. Mean normalized spectral entropy
682 across all genes was computed at each time point, and contiguous time points exceeding the
683 median were identified as candidate clusters. To assess significance, we generated a null
684 distribution of maximum cluster sizes by independently permuting each gene's entropy trace
685 1,000 times. Clusters whose size exceeded the 95th percentile of the null distribution were
686 considered significant transition epochs and visualized as shaded intervals on the mean entropy
687 trajectory.
688

689 **Statistical Analysis**

690 Data are reported as mean ± standard error of the mean (SEM) unless otherwise specified.
691 Circular phases are presented as mean ± circular standard deviation (SD). For parametric curve
692 fits, we report best fit estimate ± standard error (SE), obtained from the asymptotic covariance
693 matrix of the nonlinear least-squares fit. Statistical comparisons used unpaired or one-sample *t*-
694 tests for two-group comparisons, the Mann-Whitney U test for non-parametric comparisons
695 (**Fig. S1**), one-way ANOVA with Tukey's post hoc test for multiple groups, and two-way ANOVA

696 followed by the appropriate post hoc test for interactions over time. Linear relationships were
697 assessed using ordinary least-squares regression with the coefficient of determination (R^2) as
698 goodness of fit, and a two-sided p value. For nonlinear fits, model selection was guided by the
699 Akaike Information Criterion (AIC) and the Bayesian Information Criterion (BIC). For temperature
700 entrainment experiments (**Fig. 3F**), phase drift relative to zero was assessed using two one-sided
701 tests for equivalence (TOST; equivalence bounds ±0.483 rad/cycle) together with one-sample *t*-
702 tests. At E14, 4VCP drift was not statistically different from zero (-0.154 ± 0.109 rad/cycle, p =
703 0.254), whereas lung drift was statistically equivalent to zero (0.078 ± 0.025 rad/cycle, p = 0.053).
704 At E16, both tissues showed drift equivalent to zero (4VCP: 0.174 ± 0.089 rad/cycle, p = 0.146;
705 lung: 0.018 ± 0.010 rad/cycle, p = 0.137). At E18, the 4VCP displayed significant negative drift
706 exceeding equivalence bounds (-0.473 ± 0.042 rad/cycle, p = 0.0015), whereas the lung
707 remained equivalent to zero (0.068 ± 0.019 rad/cycle, p = 0.0396). No data were excluded as
708 outliers except in the following cases: spurious FFT-derived period estimates in non-periodic
709 time series, clear failures in RNA quantification, and dispersed amplitude or period values from
710 4VCP ROIs, where outliers were identified using the ROUT test (Q = 1%). All statistical analyses
711 were performed in GraphPad Prism 9 (GraphPad) and Mathematica 13 (Wolfram Research).
712

713 **Acknowledgements**

714 We thank Daisuke Ono (Nagoya University) for providing the *Bmal1-ELuc* mice and Lillian Byer
715 for critical reading of the manuscript. This work was supported by the National Science and
716 Technology Council (NSTC) (109-2314-B-038-071, 109-2320-B-038-020, 110-2314-B-038-162,
717 110-2311-B-038-003, 111-2314-B-038-008, 112-2314-B-038-063, 113-2314-B-038-121, 114-
718 2320-B-038-052-MY3, 114-2811-B-038-015) and the Higher Education Sprout Project of the
719 Ministry of Education (MOE) in Taiwan. Figures were created using BioRender.com.

720

721 **Competing interests**

722 The authors declare no competing interests.

723

724 **Data availability**

725 The data supporting the findings of this study are available from the corresponding author
726 upon reasonable request.

727

728 **References**

729 1. Abraham U, Granada AE, Westermark PO, Heine M, Kramer A, Herzel H (2010). Coupling
730 governs entrainment range of circadian clocks. *Mol Syst Biol*, 6:438.

731 2. Astiz M, Oster H (2021). Feto-maternal crosstalk in the development of the circadian clock
732 system. *Front Neurosci*, 14:631687.

733 3. Awatramani R, Soriano P, Rodriguez C, Mai JJ, Dymecki SM (2003). Cryptic boundaries in
734 roof plate and choroid plexus identified by intersectional gene activation. *Nat Genet*,
735 35:70-75.

736 4. Bedont JL, Blackshaw S (2015). Constructing the suprachiasmatic nucleus: a
737 watchmaker's perspective on the central clockworks. *Front Syst Neurosci*, 9:74.

738 5. Brown SA, Zumbrunn G, Fleury-Olela F, Preitner N, Schibler U (2002). Rhythms of
739 mammalian body temperature can sustain peripheral circadian clocks. *Curr Biol*, 12:1574-
740 1583.

741 6. Bueno C, Menna-Barreto L (2016). Development of sleep/wake, activity and temperature
742 rhythms in newborns maintained in a neonatal intensive care unit and the impact of
743 feeding schedules. *Infant Behav Dev*, 44:21-28.

744 7. Buhr ED, Yoo SH, Takahashi JS (2010). Temperature as a universal resetting cue for
745 mammalian circadian oscillators. *Science*, 330:379-385.

746 8. Canaple L, Gréchez-Cassiau A, Delaunay F, Dkhissi-Benyahya O, Samarut J (2018).
747 Maternal eating behavior is a major synchronizer of fetal and postnatal peripheral clocks in
748 mice. *Cell Mol Life Sci*, *75*:3991-4005.

749 9. Cao X, Yan Y, Luo X, Yang X, Cui H, Yang Y, Li H (2022). Analyses of the circadian clock
750 genes expression in whole embryos and maternal major tissues of mice. *J Mol Histol*,
751 53:473-482.

752 10. Carmona-Alcocer V, Abel JH, Sun TC, Petzold LR, Doyle FJ, Simms CL, Herzog ED
753 (2018). Ontogeny of circadian rhythms and synchrony in the suprachiasmatic nucleus. *J*
754 *Neurosci*, 38:1326-1334.

755 11. Caviness VS, Takahashi T, Nowakowski RS (1995). Numbers, time and neocortical
756 neuronogenesis: a general developmental and evolutionary model. *Trends Neurosci*,
757 18:379-383.

758 12. Čečmanová V, Houdek P, Šuchmanová K, Sládek M, Sumová A (2019). Development and
759 entrainment of the fetal clock in the suprachiasmatic nuclei: the role of glucocorticoids. *J*
760 *Biol Rhythms,* 34:307-322.

761 13. Chau KF, Springel MW, Broadbelt KG, Park HY, Topal S, Lun MP, Mullan H, Maynard T,
762 Steen H, LaMantia AS, Lehtinen MK (2015). Progressive differentiation and instructive

763 capacities of amniotic fluid and cerebrospinal fluid proteomes following neural tube
764 closure. *Dev Cell*, 35:789-802.

765 14. Courtney Y, Head JP, Dani N, Chechneva OV, Shipley FB, Zhang Y, Holtzman MJ, Sadegh
766 C, Libermann TA, Lehtinen MK (2025). Choroid plexus apocrine secretion shapes CSF
767 proteome during mouse brain development. *Nat Neurosci*, 28:1446-1459.

768 15. Daubechies I, Lu J, Wu HT (2011). Synchrosqueezed wavelet transforms: An empirical
769 mode decomposition-like tool. *Appl Comput Harmon Anal*, 30:243-261.

770 16. Davis FC, Gorski RA (1988). Development of hamster circadian rhythms: role of the
771 maternal suprachiasmatic nucleus. *J Comp Physiol A*, 162:601-610.

772 17. Dolatshad H, Cary AJ, Davis FC (2010). Differential expression of the circadian clock in
773 maternal and embryonic tissues of mice. *PLoS ONE*, 5:e9855.

774 18. Edelbo BL, Andreassen SN, Steffensen AB, MacAulay N (2023). Day-night fluctuations in
775 choroid plexus transcriptomics and cerebrospinal fluid metabolomics. *PNAS Nexus*,
776 2:pgad262.

777 19. Elmore SA, Cochran RZ, Bolon B, Lubeck B, Mahler B, Sabio D, Ward JM (2022).
778 Histology atlas of the developing mouse placenta. *Toxicol Pathol*, 50:60-117.

779 20. Ermentrout B (1996). Type I membranes, phase resetting curves, and synchrony. *Neural*
780 *Comput*, 8:979-1001.

781 21. Finger AM, Dibner C, Kramer A (2020). Coupled network of the circadian clocks: a driving
782 force of rhythmic physiology. *FEBS Lett*, 594:2734-2769.

783 22. Gato A, Moro JA, Alonso MI, Bueno D, de La Mano A, Martín C (2005). Embryonic
784 cerebrospinal fluid regulates neuroepithelial survival, proliferation, and neurogenesis in
785 chick embryos. *Anat Rec A Discov Mol Cell Evol Biol*, 284:475-484.

786 23. Ghersi-Egea JF, Strazielle N, Catala M, Silva-Vargas V, Doetsch F, Engelhardt B (2018).
787 Molecular anatomy and functions of the choroidal blood-cerebrospinal fluid barrier in
788 health and disease. *Acta Neuropathol*, 135:337-361.

789 24. Govindan RB, Andescavage NN, Basu S, Murnick J, Ngwa J, Galla JT, Kapse K,
790 Limperopoulos C, du Plessis A (2024). Circadian rhythm development in preterm infants:
791 The role of postnatal versus postmenstrual age. *Early Hum Dev*, 196:106084.

792 25. Guyer C, Huber R, Fontijn J, Bucher HU, Nicolai H, Werner H, Molinari L, Latal B, Jenni
793 OG (2015). Very preterm infants show earlier emergence of 24-hour sleep-wake rhythms
794 compared to term infants. *Early Hum Dev*, 91:37-42.

795 26. Hildyard JCW, Wells DJ, Piercy RJ (2022). Identification of qPCR reference genes suitable
796 for normalising gene expression in the developing mouse embryo. *Wellcome Open Res*,
797 6:197.

798 27. Hunter NL, Dymecki SM (2007). Molecularly and temporally separable lineages form the
799 hindbrain roof plate and contribute differentially to the choroid plexus. *Development*,
800 134:3449-3460.

801 28. Imayoshi I, Isomura A, Harima Y, Kawaguchi K, Kori H, Miyachi H, Fujiwara T, Ishidate F,
802 Kageyama R (2013). Oscillatory control of factors determining multipotency and fate in
803 mouse neural progenitors. *Science*, 342:1203-1208.

29. Jia BZ, Qi Y, Wong-Campos JD, Megason SG, Cohen AE (2023). A bioelectrical phase transition patterns the first vertebrate heartbeats. *Nature*, 622:149-155.

30. Jud C, Albrecht U (2006). Circadian rhythms in murine pups develop in absence of a functional maternal circadian clock. *J Biol Rhythms*, 21:149-154.

31. Kaiser K, Bryja V (2020). Choroid plexus: the orchestrator of long-range signalling within the CNS. *Int J Mol Sci,* 21:4760.

32. Kaneko H, Kaitsuka T, Tomizawa K (2023). Artificial induction of circadian rhythm by combining exogenous BMAL1 expression and polycomb repressive complex 2 inhibition in human induced pluripotent stem cells. *Cell Mol Life Sci*, 80:200.

33. Kowalska E, Moriggi E, Bauer C, Dibner C, Brown SA (2010). The circadian clock starts ticking at a developmentally early stage. *J Biol Rhythms*, 25:442-449.

34. Kriegstein A, Alvarez-Buylla A (2009). The glial nature of embryonic and adult neural stem cells. *Annu Rev Neurosci*, 32:149-184.

35. Lamus F, Martín C, Carnicero E, Moro JA, Fernández JMF, Mano A, Gato Á, Alonso MI (2020). FGF2/EGF contributes to brain neuroepithelial precursor proliferation and neurogenesis in rat embryos: the involvement of embryonic cerebrospinal fluid. *Dev Dyn*, 249:141-153.

36. Landgraf D, Koch CE, Oster H, Alvarez-Bolado G, Pombal MA (2014). Embryonic development of circadian clocks in the mammalian suprachiasmatic nuclei. *Front Neuroanat,* 8:143.

824 37. Langford MB, O'Leary CJ, Veeraval L, White A, Lanoue V, Cooper HM (2020). WNT5a
825 regulates epithelial morphogenesis in the developing choroid plexus. *Cereb Cortex*,
826 30:3617-3631.

827 38. Lehtinen MK, Zappaterra MW, Chen X, Yang YJ, Hill AD, Lun M, Maynard T, Gonzalez D,
828 Kim S, Ye P, D'Ercole AJ, Wong ET, LaMantia AS, Walsh CA (2011). The cerebrospinal
829 fluid provides a proliferative niche for neural progenitor cells. *Neuron*, 69:893-905.

830 39. Liška K, Sládek M, Čečmanová V, Sumová A (2021). Glucocorticoids reset circadian clock
831 in choroid plexus via period genes. *J Endocrinol*, 248:155-166.

832 40. Lun MP, Monuki ES, Lehtinen MK (2015). Development and functions of the choroid
833 plexus-cerebrospinal fluid system. *Nat Rev Neurosci*, 16:445-457.

834 41. Martin C, Alonso MI, Santiago C, Moro JA, de la Mano A, Carretero R, Gato A (2009). Early
835 embryonic brain development in rats requires the trophic influence of cerebrospinal fluid.
836 *Int J Dev Neurosci*, 27:733-740.

837 42. Mauvoisin D, Wang J, Jouffe C, Martin E, Atger F, Waridel P, Quadroni M, Gachon F, Naef
838 F (2014). Circadian clock-dependent and -independent rhythmic proteomes implement
839 distinct diurnal functions in mouse liver. *Proc Natl Acad Sci USA*, 111:167-172

840 43. Mei M, Xiang RL, Cong X, Zhang Y, Li J, Yi X, Park K, Han JY, Wu LL, Yu GY (2015).
841 Claudin-3 is required for modulation of paracellular permeability by TNF-α through
842 ERK1/2/slug signaling axis in submandibular gland. *Cell Signal*, 27:1915-1927.

843 44. Miyan JA, Nabiyouni M, Zendah M (2003). Development of the brain: a vital role for
844 cerebrospinal fluid. *Can J Physiol Pharmacol*, 81:317-328.

845 45. Murayama Y, Kori H, Oshima C, Kondo T, Iwasaki H, Ito H (2017). Low temperature
846 nullifies the circadian clock in cyanobacteria through Hopf bifurcation. *Proc Natl Acad Sci*
847 *USA*, 114:5641-5646.

848 46. Myung J, Schmal C, Hong S, Tsukizawa Y, Rose P, Zhang Y, Holtzman MJ, De Schutter E,
849 Herzel H, Takumi T (2018). The choroid plexus is an important circadian clock component.
850 *Nat Commun*, 9:1-13.

851 47. Myung J, Vitet, H, Truong VH, Ananthasubramaniam B (2025). The role of the multiplicity
852 of circadian clocks in mammalian systems. *Sleep Med*, 131:106518.

853 48. Nakajima Y, Yamazaki T, Nishii S, Noguchi T, Hoshino H, Niwa K, Viviani VR, Ohmiya Y
854 (2010). Enhanced beetle luciferase for high-resolution bioluminescence imaging. *PLoS*
855 *ONE*, 5:e10011.

856 49. Oh-oka K, Kono H, Ishimaru K, Miyake K, Kubota T, Ogawa H, Okumura K, Shibata S,
857 Nakao A (2014). Expressions of tight junction proteins occludin and claudin-1 are under
858 the circadian control in the mouse large intestine: Implications in intestinal permeability
859 and susceptibility to colitis. *PLoS ONE*, 9:e98016.

860 50. Qian L, Gu Y, Zhai Q, Xue Z, Liu Y, Li S, Zeng Y, Sun R, Zhang Q, Cai X, Ge W, Dong Z,
861 Gao H, Zhou Y, Zhu Y, Xu Y, Guo T (2023). Multitissue Circadian Proteome Atlas of WT
862 and Per1-/-/Per2-/- Mice. *Mol Cell Proteomics*, 22:100675.

863 51. Robles MS, Cox J, Mann M (2014). In-Vivo Quantitative Proteomics Reveals a Key
864 Contribution of Post-Transcriptional Mechanisms to the Circadian Regulation of Liver
865 Metabolism. *PLoS Genet*, 10:e1004047.

866 52. Salvante KG, Milano K, Kliman HJ, Nepomnaschy PA (2017). Placental 11 β-
867 hydroxysteroid dehydrogenase type 2 (11β-HSD2) expression very early during human
868 pregnancy. *J Dev Orig Health Dis,* 8:149-154.

869 53. Saunders NR, Dziegielewska KM, Fame RM, Lehtinen MK, Liddelow SA (2023). The
870 choroid plexus: A missing link in our understanding of brain development and function.
871 *Physiol Rev*, 103:919-956.

872 54. Serón-Ferré M, Mendez N, Abarzua-Catalan L, Vilches N, Valenzuela FJ, Reynolds HE,
873 Llanos AJ, Rojas A, Valenzuela GJ, Torres-Farfan C (2012). Circadian rhythms in the fetus.
874 *Mol Cell Endocrinol*, 349:68-75.

875 55. Smarr BL, Zucker I, Kriegsfeld LJ (2016). Detection of successful and unsuccessful
876 pregnancies in mice within hours of pairing through frequency analysis of high temporal
877 resolution core body temperature data. *PLoS ONE*, 11:e0160127.

878 56. Steinemann A, Galm I, Chip S, Nitsch C, Maly IP (2016). Claudin-1, -2 and -3 are
879 selectively expressed in the epithelia of the choroid plexus of the mouse from early
880 development and into adulthood while claudin-5 is restricted to endothelial cells. *Front.*
881 *Neuroanat*, 10:16.

882 57. Subashini C, Dhanesh SB, Chen CM, Riya PA, Meera V, Divya TS, Kuruvilla R, Buttler K,
883 James J (2017). Wnt5a is a crucial regulator of neurogenesis during cerebellum
884 development. *Sci Rep*, 7:42523.

885 58. Truong VH, Myung J (2023). LocoBox: Modular hardware and open-source software for
886 circadian entrainment and behavioral monitoring in home cages. *Sensors*, 23:9469.

887 59. Ukai-Tadenuma M, Kasukawa T, Ueda HR (2008). Proof-by-synthesis of the transcriptional
888 logic of mammalian circadian clocks. *Nat Cell Biol*, 10:1154-1163.

889 60. Umemura Y, Koike N, Ohashi M, Tsuchiya Y, Meng QJ, Minami Y, Hara M, Hisatomi M,
890 Yagita K (2017). Involvement of posttranscriptional regulation of Clock in the emergence of
891 circadian clock oscillation during mouse development. *Proc Natl Acad Sci USA*,
892 114:E7479-E7488.

893 61. Umemura Y, Koike N, Tsuchiya Y, Watanabe H, Kondoh G, Kageyama R, Yagita K (2022).
894 Circadian key component CLOCK/BMAL1 interferes with segmentation clock in mouse
895 embryonic organoids. *Proc Natl Acad Sci USA*, 119:e2114083119.

896 62. VanDunk C, Hunter LA, Gray PA (2011). Development, maturation, and necessity of
897 transcription factors in the mouse suprachiasmatic nucleus. *J Neurosci*, 31:6457-6467.

898 63. Wharfe MD, Mark PJ, Wyrwoll CS, Smith JT, Yap C, Clarke MW, Waddell BJ (2016).
899 Pregnancy-induced adaptations of the central circadian clock and maternal
900 glucocorticoids. *J Endocrinol*, 228:135-147.

901 64. Wong SD, Wright KP, Spencer RL, Vetter C, Hicks LM, Jenni OG, LeBourgeois MK (2022).
902 Development of the circadian system in early life: maternal and environmental factors. *J*
903 *Physiol Anthropol*, 41:22.

904 65. Wreschnig D, Dolatshad H, Davis FC (2014). Embryonic development of circadian
905 oscillations in the mouse hypothalamus. *J Biol Rhythms*, 29:299-310.

906 66. Wolburg H, Wolburg-Buchholz K, Liebner S, Engelhardt B (2001) Claudin-1, claudin-2 and
907 claudin-11 are present in tight junctions of choroid plexus epithelium of the mouse.
908 *Neurosci Lett*, 307:77-80.

909 67. Yagita K, Horie K, Koinuma S, Nakamura W, Yamanaka I, Urasaki A, Shigeyoshi Y,
910 Kawakami K, Shimada S, Takeda J, Uchiyama Y (2010). Development of the circadian
911 oscillator during differentiation of mouse embryonic stem cells in vitro. *Proc Natl Acad Sci*
912 *USA*, 107:3846-3851.

913 68. Yagita K (2024). Emergence of the circadian clock oscillation during the developmental
914 process in mammals. *Curr Opin Genet Dev*, 84:102152.

915 69. Yaw AM, Duong TV, Nguyen D, Hoffmann HM (2021). Circadian rhythms in the mouse
916 reproductive axis during the estrous cycle and pregnancy. *J Neurosci Res*, 99:294-308.

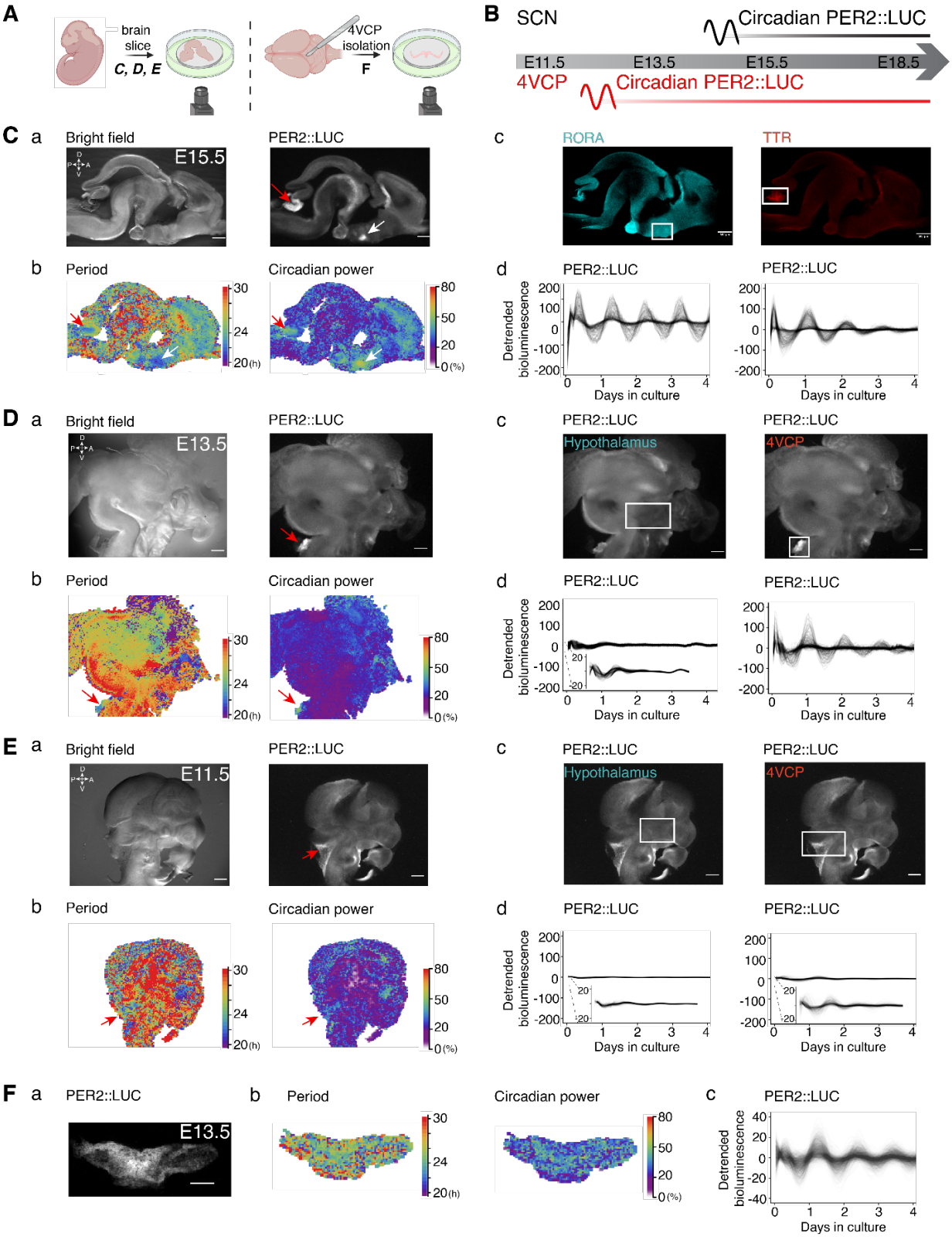

Figure 1. Location of the first clock in the mouse embryonic brain. (**A**) Workflow of PER2::LUC bioluminescence recording from embryonic brain/head slices (left; C-E) or

920 isolated 4VCP explants (right; F). (**B**) Developmental timeline summarizing that 4VCP
921 PER2::LUC rhythms precede those in the SCN. (**C**) E15.5 PER2::LUC brain slice. **a**: Bright-
922 field (left) and bioluminescence (right) images. **b**: Maps of FFT-derived period (left) and
923 circadian power (right; see Materials and Methods). **c**: Post hoc immunofluorescence for
924 RORA (left) and the CP marker TTR (right) after tissue clearing. **d**: Detrended PER2::LUC time
925 series from the regions indicated by white boxes in Cc; see **Movie S1**. Representative of 3
926 experiments (5 slices total). (**D**) E13.5 PER2::LUC head slice. **a**: Bright-field (left) and
927 bioluminescence (right) images. **b**: Period (left) and circadian power (right) maps as in Cb. **c**:
928 White boxes indicate the putative hypothalamus/SCN region (left) and 4VCP (right). **d**:
929 Detrended time series from the regions in Dc; see **Movie S2**. Representative of 3 experiments
930 (4 slices total). (**E**) E11.5 PER2::LUC head slice. **a**: Bright-field (left) and bioluminescence
931 (right) images. **b**: Period (left) and circadian power (right) maps. **c**: White boxes indicate
932 putative hypothalamus (left) and 4VCP (right). **d**: Detrended time series from the regions in
933 Ec; see **Movie S3**. Representative of 3 experiments (3 slices total). (**F**) Isolated E13.5
934 PER2::LUC 4VCP explant. **a**: Bioluminescence image. **b**: Period (left) and circadian power
935 (right) maps. **c**: Detrended time series over 4 days; see **Movie S4**. Representative of 4
936 experiments (7 explants total). Throughout, red arrows indicate the 4VCP; white arrows
937 indicate the SCN. Scale bar: 500 μm.

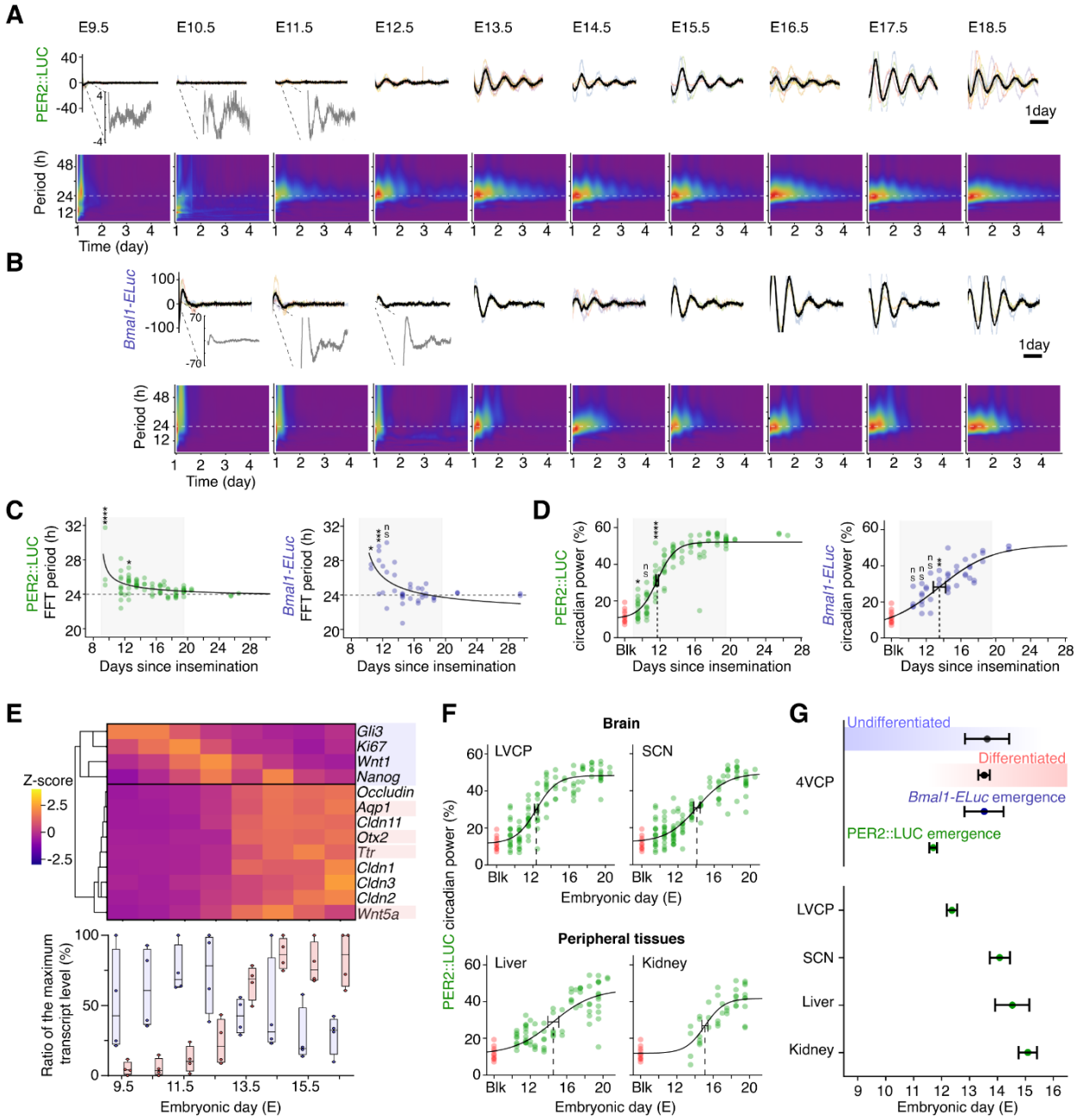

Figure 2. Quantification of clock emergence in brain and peripheral tissues, and characterization of 4VCP differentiation. (**A**) Individual (thin colored) and mean (black) detrended PER2::LUC bioluminescence traces (top) and spectrograms (bottom) from the embryonic 4VCP, E9.5 to E18.5. Zoom-in insets highlight low-amplitude rhythms at early stages. (**B**) As in (A), for *Bmal1-ELuc*, from E10.5 to E18.5. (**C**) Period scatter plots for PER2::LUC (left) and *Bmal1-ELuc* (right) with $1/\sqrt{(t - t_0)}$ fits. Asterisks indicate significant differences from 24 h (ns, not significant; $^*p < 0.05$; $^{***}p < 0.001$; $^{****}p < 0.0001$). (**D**) Circadian power scatter plots for PER2::LUC (left) and *Bmal1-ELuc* (right) with sigmoidal fits;

947 emergence times (T_e) were E11.7 ± 0.1 and E13.5 ± 0.7, respectively (best fit estimate ± SE).
948 Asterisks indicate significant differences from 20% (as in (C)). (**E**) Heatmap of developmental
949 marker genes (top) and box-and-whisker plots (bottom) comparing stem/progenitor (blue)
950 and differentiation (red) markers across embryonic stages; each gene is normalized to its
951 maximum expression between E9.5 and E16.5. Each data point represents the mean of 6-16
952 litters (3-11 embryos per litter). Boxes show interquartile range (25th and 75th percentile) and
953 median; whiskers indicate minimum and maximum values. (**F**) Developmental trajectories of
954 PER2::LUC circadian power in the LVCP and the SCN (top) and liver and kidney (bottom),
955 with sigmoidal fits. (**G**) Comparison of half-maximal times for progenitor markers (E13.6 ±
956 0.8) and differentiation markers (E13.5 ± 0.2) with emergence times of *Bmal1-ELuc* and
957 PER2::LUC oscillations in the 4VCP, and PER2::LUC emergence time for each tissue. Error
958 bars: mean ± SEM after outlier exclusion.

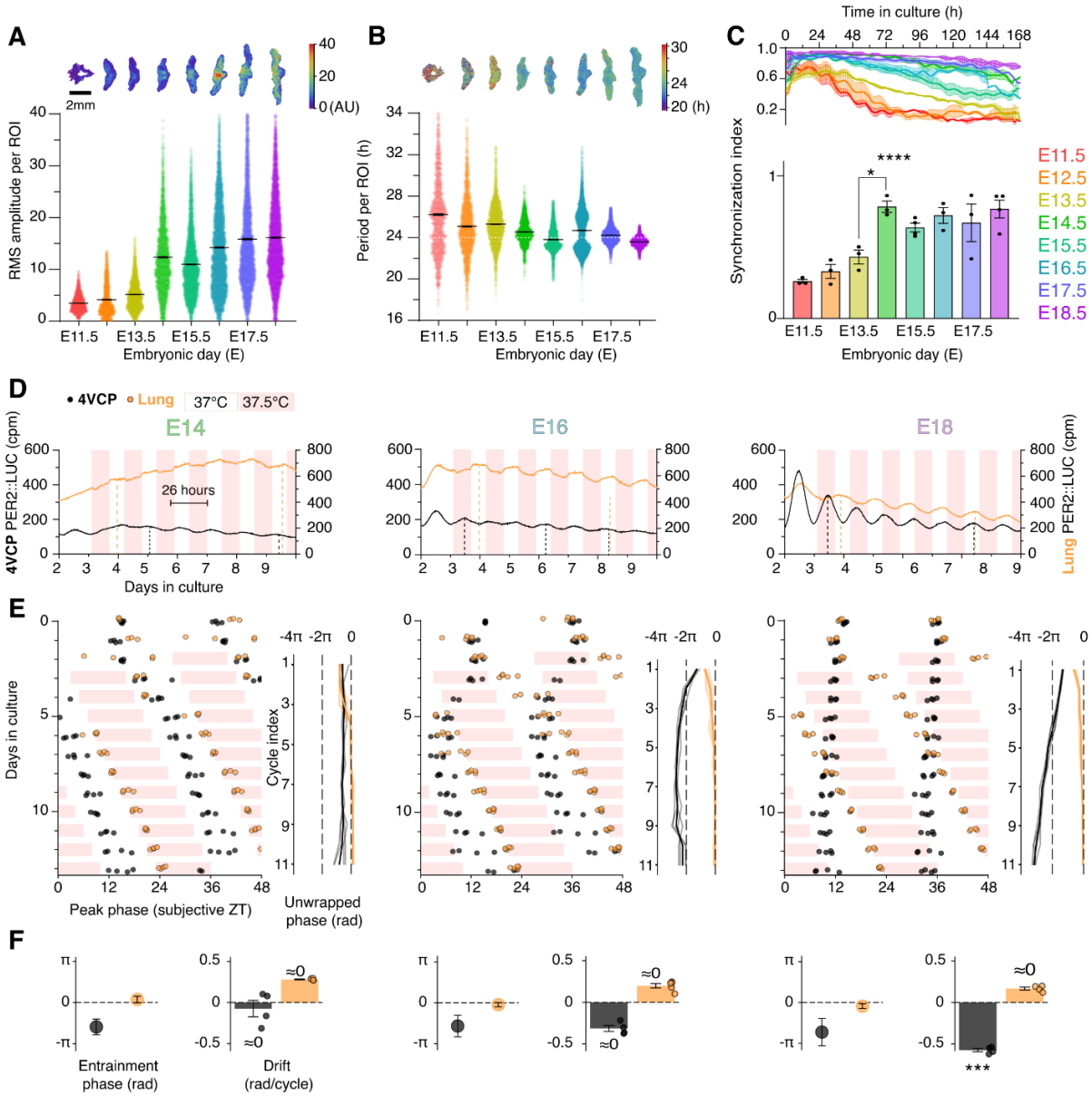

Figure 3. Characterization of the bifurcation type describing the onset of the embryonic 4VCP clock. (**A**) Single-cell RMS amplitude and (**B**) period of PER2::LUC in the embryonic 4VCP from E11.5 to E18.5. Insets above each panel show representative spatial maps across stages (scale bar: 2 mm). n = 579-2,787 ROIs from 3-4 4VCP explants and 2-3 litters per stage, after outlier exclusion. White dotted line indicates 24 h. (**C**) Synchronization index (Kuramoto order parameter) in the embryonic 4VCP explant, as it evolves over days in culture (top) and time-averaged individual values across stages, overlaid with scatter plots (bottom; same n as in (A)). One-way ANOVA ($F(7,18) = 10.72$, $p < 0.0001$) with Tukey's post hoc test (*$p = 0.0194$, ****$p < 0.0001$). (**D**) Representative raw PER2::LUC time series from the 4VCP (black) and lung (orange) at E14 (left), E16 (middle), and E18 (right). Pale red shading indicates

970 37.5 °C epochs. (**E**) Double-plots of PER2::LUC peak phase from the corresponding
971 explants, alongside unwrapped phase plots (rad). (**F**) Entrainment phase (rad) and phase drift
972 (rad/cycle) for the 4VCP and lung across the three developmental stages. Phase drift was
973 assessed using equivalence testing (TOST; bounds ±0.483 rad/cycle) together with one-
974 sample *t*-tests (see Methods). At E18, 4VCP displayed significant negative drift (-0.473 ±
975 0.042 rad/cycle, $p = 0.0015$), whereas the lung remained equivalent to zero. Error bars: mean
976 ± SEM after outlier exclusion.

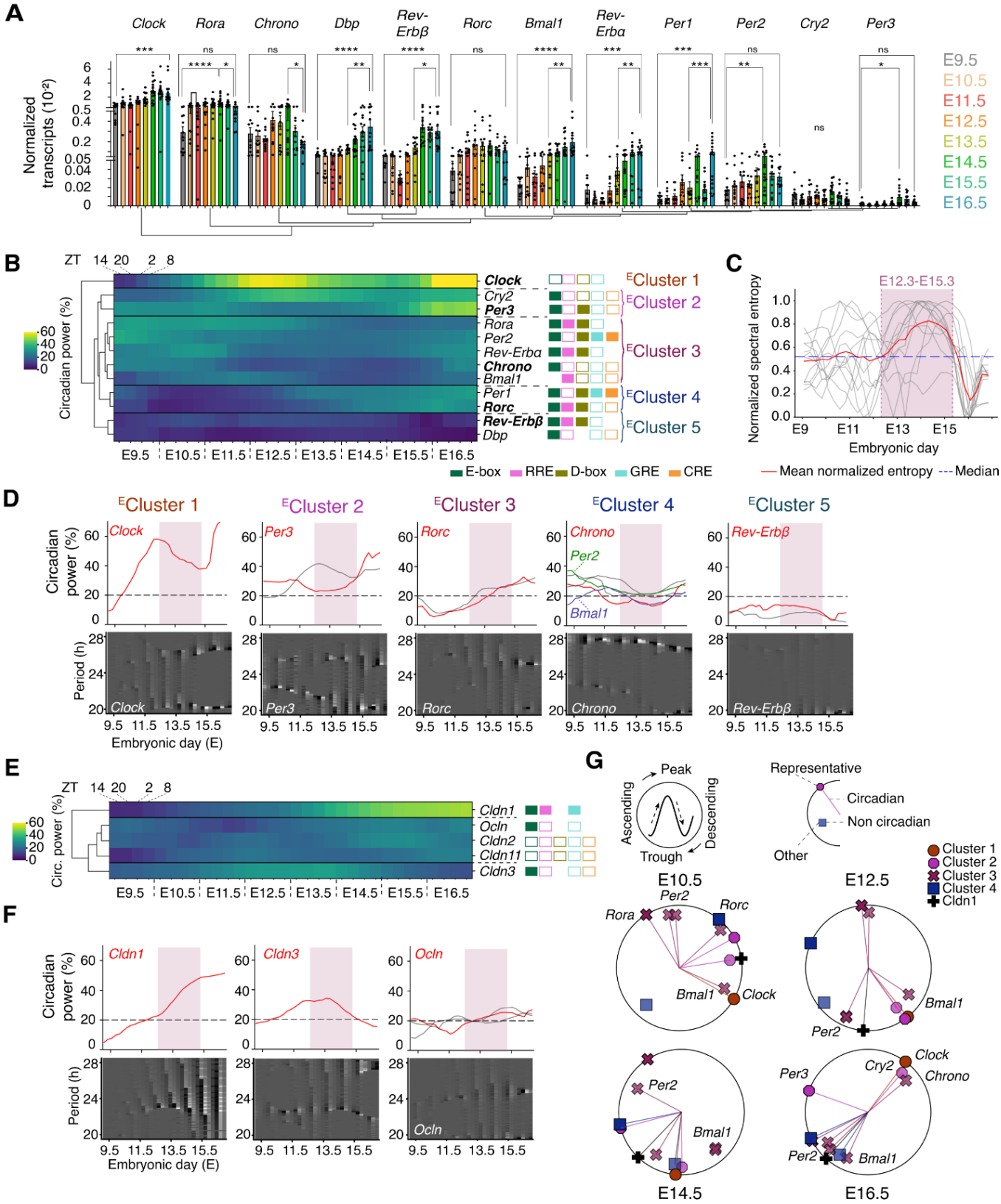
A
Clock
Rora
Chrono
Dbp
Rev-Erbβ
Rorc
Bmal1
Rev-Erbα
Per1
Per2
Cry2
Per3
Normalized transcripts (10⁻²)
E9.5
E10.5
E11.5
E12.5
E13.5
E14.5
E15.5
E16.5
B
ZT 14 20 2 8
Circadian power (%)
Clock
Cry2
Per3
Rora
Per2
Rev-Erbα
Chrono
Bmal1
Per1
Rorc
Rev-Erbβ
Dbp
ECluster 1
ECluster 2
ECluster 3
ECluster 4
ECluster 5
E-box
RRE
D-box
GRE
CRE
C
E12.3-E15.3
Normalized spectral entropy
Embryonic day
Mean normalized entropy
Median
D
ECluster 1
ECluster 2
ECluster 3
ECluster 4
ECluster 5
Circadian power (%)
Period (h)
Embryonic day (E)
E
Circ. power (%)
Cldn1
Ocln
Cldn2
Cldn11
Cldn3
F
G
Peak
Trough
Ascending
Descending
Representative
Circadian
Non circadian
Other
Cluster 1
Cluster 2
Cluster 3
Cluster 4
Cldn1
E10.5
E12.5
E14.5
E16.5

977

Figure 4. Rhythmic expression of clock genes in the embryonic 4VCP across development. (**A**) Normalized mRNA abundance of core clock genes in the embryonic 4VCP from E9 to E16 (n = 8-25 litters per stage). One-way ANOVA followed by Tukey's post hoc test (ns, not significant; $^{*}p < 0.05$; $^{**}p < 0.01$; $^{***}p < 0.001$; $^{****}p < 0.0001$). (**B**) Hierarchical clustering and heatmap of embryonic circadian power of clock genes across stages and ZT. Tiles on the right annotate promoter-motif classes: filled tiles indicate validated motifs; outlined tiles indicate predictions (see **Fig. S7B**). Each data point represents the mean of 2-5 litters (3-11 embryos per litter). (**C**) Normalized spectral entropy across embryonic days. The mean entropy (red line) is plotted against the overall median (blue dashed line). The shaded region marks significant high-entropy epochs identified by permutation clustering: contiguous periods above the median that exceed the 95th percentile of cluster sizes from 1,000 random permutations (E12.3-E15.3). (**D**) Circadian power trajectories for each clock gene, grouped by cluster (top; representative gene in red; dashed line, 20% detection threshold). Shaded overlays indicate the high-entropy epoch (E12.3-E15.3). Circadian phase-weighted power spectrograms for the representative gene of each cluster across embryonic days (bottom). (**E**) As in (B), for tight junction genes (see also **Fig. S9B**). Each data point represents the mean of 1-4 litters. (**F**) As in (D), for tight junction genes. (**G**) Circular phase plots of embryonic gene expression across developmental stages. Peak phase is at 12 o'clock; phase rotates clockwise. Genes with circadian power ≥ 20% are connected to the center by lines and shown as opaque markers on the circle; non-circadian genes (< 20%) are shown as filled squares. Marker shape and color indicate cluster membership; the representative gene of each cluster is positioned on the outer radius. "^{E}Cluster" denotes clusters derived from embryonic tissues. Error bars: mean ± SEM after outlier exclusion.

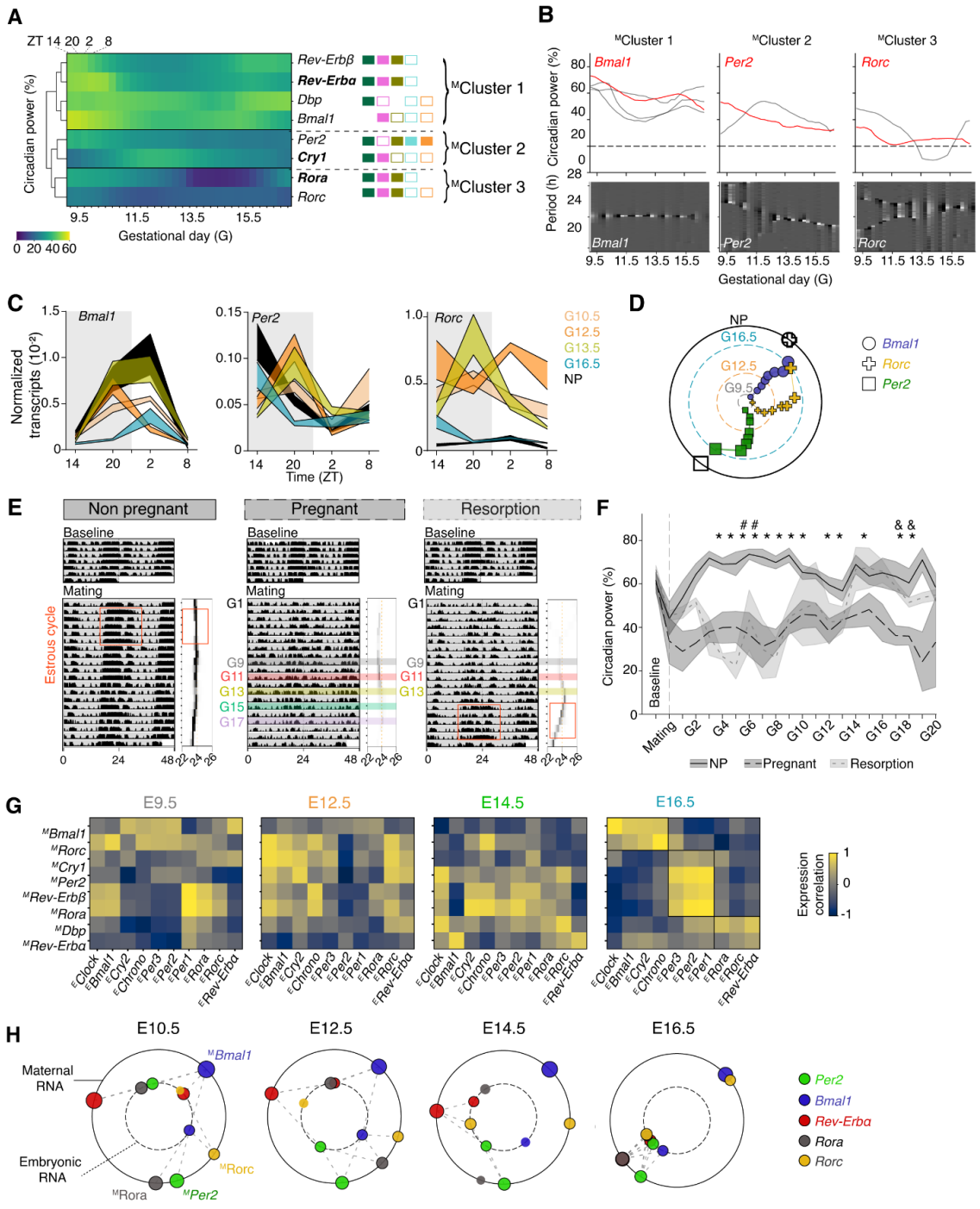

Figure 5. Maternal clock and maternal-embryonic transcriptional coordination across development. (**A**) Hierarchical clustering and heatmap of circadian power of maternal clock genes across gestational days and ZT. Tiles on the right annotate promoter-motif classes: filled tiles indicate validated motifs; outlined tiles indicate predictions (see **Fig. S7B**). Each data point represents the mean of 2-4 dams. (**B**) Circadian power trajectories for each maternal clock gene, grouped by cluster (top; representative gene in red; dashed line, 20%

detection threshold). Circadian phase-weighted power spectrogram for *Bmal1, Per2* and *Rorc* across gestational days (bottom). (**C**) Normalized mRNA abundance of maternal *Bmal1*, *Per2* and *Rorc* across ZT at gestational days G10.5, G12.5, G13.5, and G16.5 (n = 2-4 dams) and in non-pregnant (NP) females (n = 3-5; black). Full time courses from G9.5 to G16.5 are shown in **Fig. S10B**. (**D**) Phase plot of maternal *Bmal1* (circle), *Per2* (square), and *Rorc* (cross) mRNA expression compared with non-pregnant female mice. Inner ring: G9.5 (grey), G12.5 (orange), and G16.5 (blue); outer ring: non-pregnant mice (NP). (**E**) Representative double-plotted actograms of a non-pregnant mouse, a pregnant mouse, and a pregnant mouse undergoing spontaneous resorption in DD (top: baseline before mating; bottom: after mating), with period and spectral power indicated by shading intensity (right panels; darker = higher power). (**F**) Circadian power of maternal locomotor activity throughout pregnancy (n = 5), spontaneous resorption (n = 2), and non-pregnant controls (n = 5). Two-sample t-test: *pregnant vs. non-pregnant ($-5.4 < t < -2.8$; $0.001 < p < 0.035$); #non-pregnant vs. resorption (t = 11.4, p = 0.0001 at G4; t = 4.3, p = 0.047 at G5), &pregnant vs. resorption (t = -3.7; p = 0.014 at G17; t = -2.7, p = 0.043 at G18). (**G**) Heatmaps of pairwise correlation between maternal and embryonic clock genes at E9.5, E12.5, E14.5, and E16.5. (**H**) Dual-radius phase plots of maternal and embryonic gene expression across stages. Inner ring: embryonic cluster representatives; outer ring: selected maternal genes. Dotted lines connect maternal-embryonic pairs when both exhibit circadian power ≥ 20% and their phase difference is < $\pi/2$ rad (≤ 6 h). "^{M}Cluster" denotes a cluster derived from maternal tissue. Error bars: mean ± SEM after outlier exclusion.

Supplementary Materials

	GenBank Accession	NCBI GeneID	Gene name	T_m (°C)	Primer sequence (5'-3')	Primer length
Genes used for normalization	NM_007393	11461	*Actb-c16X*, forward	64.6	GCCCTGAGGCTCTTTTCCAG	20
			Actb-c16X, reverse	63.8	TGCCACAGGATTCCATACCC	20
	NM_008084	14433	*Gapdh-4*, forward	62.6	AGGTCGGTGTGAACGGATTTG	21
			Gapdh-4, reverse	60.2	TGTAGACCATGTAGTTGAGGTCA	23
	NM_009438	22121	*Rpl13a*, forward	60.5	AGCCTACCAGAAAGTTTGCTTAC	23
			Rpl13a, reverse	61.0	GCTTCTTCTTCCGATAGTGCATC	23
4VCP positive genes	NM_008963	19215	*Ptgds*, forward	63.1	AATGGCTGCTCTTCGCATG	19
			Ptgds, reverse	64.8	GCCCCAGGAACTTGTCTTGTT	21
	NM_013697	22139	*Ttr*, forward	62.9	TTGCCTCGCTGGACTGGTA	19
			Ttr, reverse	61.8	TTACAGCCACGTCTACAGCAG	21
	NM_144841	18424	*Otx2*, forward	62.2	GAATCCAGGGTGCAGGTATGG	21
			Otx2, reverse	62.4	CTGAACTCACTTCCCGAGCTG	21
	NM_134110	246133	*Kcne2*, forward	60.8	CCACATTAGCCAATTTGACCCA	22
			Kcne2, reverse	62.4	CTCGGCTGTCGTGTTCCTC	19
4VCP negative genes	NM_008235	15205	*Hes1*, forward	62.2	CCAGCCAGTGTCAACACGA	19
			Hes1, reverse	61.0	AATGCCGGGAGCTATCTTTCT	21
	NM_010710	16870	*Lhx2*, forward	64.9	GCCGAGAAAGCGCAAGAGT	19
			Lhx2, reverse	64.3	TGTTCAGCATCGTTCTCGTTACA	23
	NM_008130	14634	*Gli3*, forward	62.4	CACAGCTCTACGGCGACTG	19
			Gli3, reverse	62.8	CTGCATAGTGATTGCGTTTCTTC	23
Clock genes	NM_007489	11865	*Bmal1*, forward	66.1	GCAGTGCCACTGACTACCAAGA	22
			Bmal1, reverse	62.8	TCCTGGACATTGCATTGCAT	20
	NM_011066	18627	*Per2*, forward	60.0	GAAAGCTGTCACCACCATAGAA	22
			Per2, reverse	60.5	AACTCGCACTTCCTTTTCAGG	21
	NM_007771	12952	*Cry1*, forward	64.7	AGAGGGCTAGGTCTTCTCGC	20

			Cry1, reverse	63.4	CTACAGCTCGGGACGTTCTC	20
	NM_007715	12753	*Clock*, forward	63.7	GTCCTTCAGCAGTCAGTCCAT	21
			Clock, reverse	63.7	GCCTCTATCATCCGTGTCCG	20
	NM_145434	217166	*Rev-Erbα* (*Nr1d1*), forward	65.8	TGGCCTCAGGCTTCCACTATG	21
			Rev-Erbα (*Nr1d1*), reverse	64.2	CCGTTGCTTCTCTCTCTTGGG	21
	NM_011584	353187	*Rev-Erbβ* (*Nr1d2*), forward	61.8	CCCAAGAACGCTGATATCTCTAG	23
			Rev-Erbβ (*Nr1d2*), reverse	62.1	ACACAGTAGAACCATGCCAC	20
	NM_013646	19883	*Rora*, forward	62.0	TCCAAATCCCACCTGGAAAC	20
			Rora, reverse	63.1	GGAAGGTCTGCCACGTTATCTG	22
	NM_011281	19885	*Rorc*, forward	60.6	TCCTGCCACCTTGAGTATAGTC	22
			Rorc, reverse	62.1	GTAAGTTGGCCGTCAGTGCTA	21
	NM_001352	1628	*Dbp*, forward	68.0	AATGACCTTTGAACCTGATCCCGCT	25
			Dbp, reverse	65.3	GCTCCAGTACTTCTCATCCTTCTGT	25
	NM_001033302	229599	*Chrono*, forward	61.6	GGAGACGAGTCTGAACACCC	20
			Chrono, reverse	62.4	GGGGCCGTATGAACCCTTG	19
	NM_009963	12953	*Cry2*, forward	64.2	GTCTGTGGGCATCAACCGA	19
			Cry2, reverse	64.3	TGCATCCCGTTCTTTCCCAA	20
	NM_001159367	18626	*Per1*, forward	62.6	CCCAGCTTTACCTGCAGAAG	20
			Per1, reverse	63.2	ATGGTCGAAAGGAAGCCTCT	20
	NM_011067	18628	*Per3*, forward	63.7	CACTTTGTCGACCTGCTTGC	20
			Per3, reverse	61.0	ATGAACCAAATAGGGGAGGAT	21
Tight junction genes	NM_016674	12737	*Cldn1*, forward	62.7	GGGGACAACATCGTGACCG	19
			Cldn1, reverse	61.1	AGGAGTCGAAGACTTTGCACT	21

	NM_016675	12738	*Cldn2*, forward	60.9	CAACTGGTGGGCTACATCCTA	21
			Cldn2, reverse	61.8	ATCCAGAGGCCCTTGGAAAAG	21
	NM_009902	12739	*Cldn3*, forward	62.3	ACCAACTGCGTACAAGACGAG	21
			Cldn3, reverse	62.6	CAGAGCCGCCAACAGGAAA	19
	NM_008770	18417	*Cldn11*, forward	62.1	ATGGTAGCCACTTGCCTTCAG	21
			Cldn11, reverse	61.2	AGTTCGTCCATTTTTCGGCAG	21
	NM_008756	18260	*Ocln*, forward	61.0	CTGGATCTATGTACGGCTCACA	22
			Ocln, reverse	61.1	TCCACGTAGAGACCAGTACCT	21
Development genes	NM_001256224	22418	*Wnt5a*, forward	62.6	CAACTGGCAGGACTTTCTCAA	21
			Wnt5a, reverse	63.7	CATCTCCGATGCCGGAACT	19
	NM_028016	71950	*Nanog*, forward	62.8	TCTTCCTGGTCCCCACAGTTT	21
			Nanog, reverse	60.1	GCAAGAATAGTTCTCGGGATGAA	23
	NM_001081117	17345	*Ki67*, forward	61.2	ATCATTGACCGCTCCTTTAGGT	22
			Ki67, reverse	62.0	GCTCGCCTTGATGGTTCCT	19
	NM_021279	22408	*Wnt1*, forward	60.4	GGTTTCTACTACGTTGCTACTGG	23
			Wnt1, reverse	62.3	GGAATCCGTCAACAGGTTCGT	21
	NM_007472	11826	*Aqp1*, forward	60.8	AGGCTTCAATTACCCACTGGA	21
			Aqp1, reverse	61.7	CTTTGGGCCAGAGTAGCGAT	20

Table S1. Primer sequences used for qPCR. T_m indicates melting temperature.

	E14	E16	E18	P0
4VCP	-1.83 ± 0.47 (*n* = 5)	-1.87 ± 0.70 (*n* = 4)	-1.82 ± 1.16 (*n* = 4)	2.86 ± 1.29 (*n* = 5)
SCN	-0.77 ± 0.76 (*n* = 5)	-1.3 ± 0.47 (*n* = 5)	-1.8 ± 1.05 (*n* = 5)	-0.93 ± 1.21 (*n* = 5)
LVCP	-1.03 ± 1.47 (*n* = 5)	-1.38 ± 1.44 (*n* = 5)	-0.46 ± 1.07 (*n* = 4)	-2.15 ± 1.09 (*n* = 5)
Lung	-0.02 ± 0.41 (*n* = 5)	-0.2 ± 0.3 (*n* = 5)	-0.34 ± 0.22 (*n* = 4)	-0.04 ± 0.54 (*n* = 5)

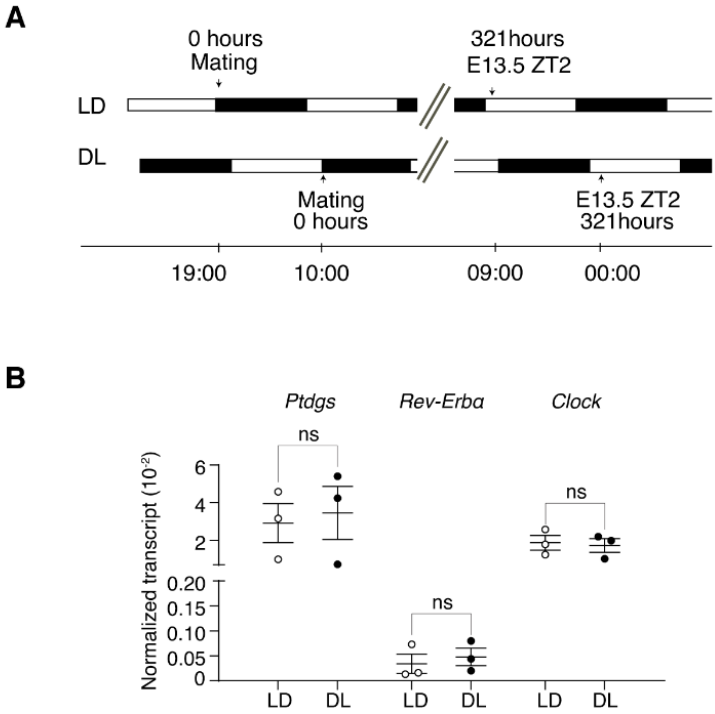

Table S2. Phase of entrainment (rad) under a 26 h temperature cycle. Shown are circular mean ± circular SD from 4-5 explants. For each explant, peak phase was averaged over the final 7 days of recording under the 26 h cycle (0 rad defined as the onset of the 37.5 °C epoch; *n*: number of explants). Negative values indicate phase lead relative to 0 rad.

1038 **Figure S1. Comparison of mRNA expression between LD and DL protocols.** (**A**) Scheme
1039 of the light-dark schedules for LD and DL (reversed-LD) conditions. (**B**) Normalized mRNA
1040 abundance of three representative genes (*Ptgds*, *Rev-erba*, *Clock*) out of 22 tested, in the
1041 embryonic 4VCP sampled at the same ZT (ZT2) from 3 pregnant mice per condition. Mann-
1042 Whitney U test; ns, not significant. Error bars: mean ± SEM.

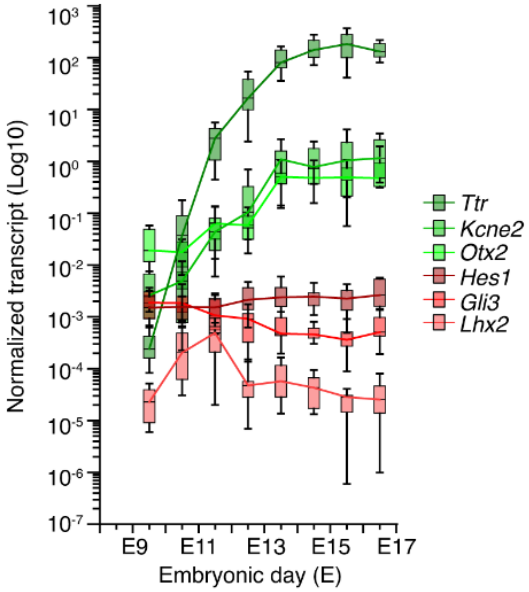

1043

1044 **Figure S2. Molecular validation of 4VCP dissection across embryonic stages.**
1045 Normalized mRNA abundance of selected 4VCP-positive (*Ttr*, *Kcne2*, *Otx2*; green) and
1046 4VCP-negative (*Gli3*, *Lhx2*, *Hes1*; red) markers in the embryonic 4VCP ($n \geq 8$ litters per stage).
1047 Data are plotted on a $\log_{10}$ scale; box-and-whisker plots show the 10th-90th percentiles.

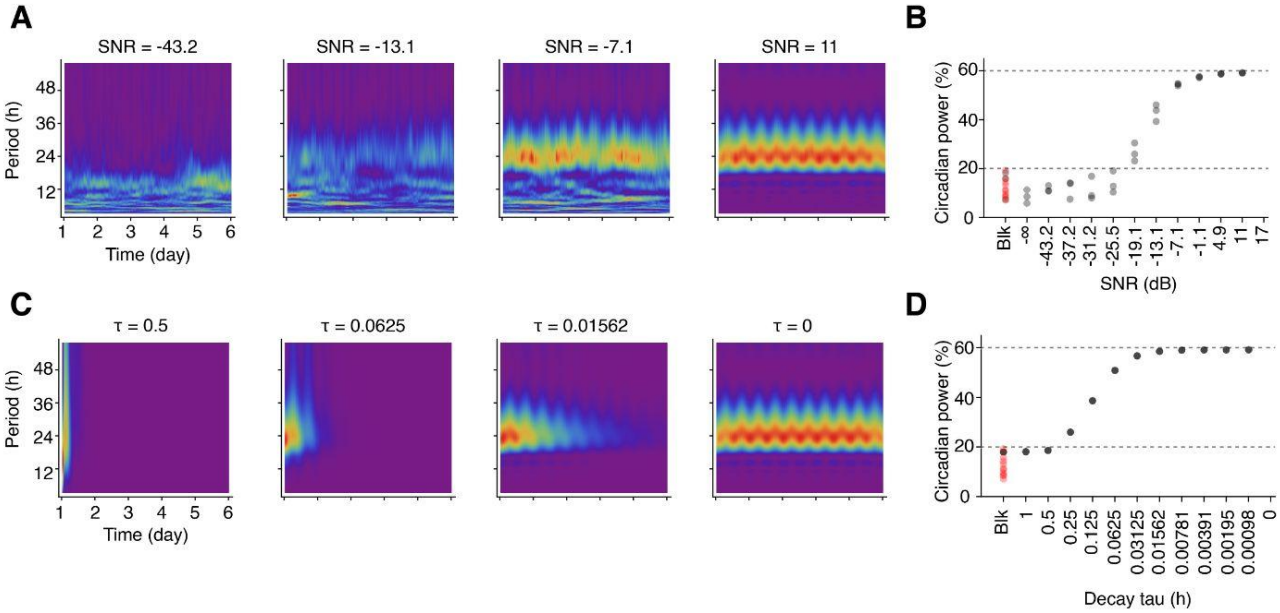

Figure S3. Quantification of circadian power in simulated bioluminescence time series. (**A**) Spectrograms from 2-day sliding-window FFT of simulated 24-h oscillations with varying noise levels, expressed as signal-to-noise ratio (SNR, dB). Increasing SNR progressively reveals the circadian peak at ~24 h. (**B**) Circadian power as a function of SNR. Each point represents one simulation. Detectable circadian rhythms fall between 20% (detection threshold) and 60% (ceiling), indicated by dashed lines. Blank recordings (Blk) from actual experiments fall below 20%. (**C**) Spectrograms of simulated 24 h oscillations with varying damping time constants (τ). Shorter τ produces stronger damping and loss of rhythmicity. (**D**) Circadian power as a function of τ. Semi-transparent points represent individual simulations but overlap substantially. As in (B), circadian rhythms below the 20% threshold (dashed line) are considered non-detectable.

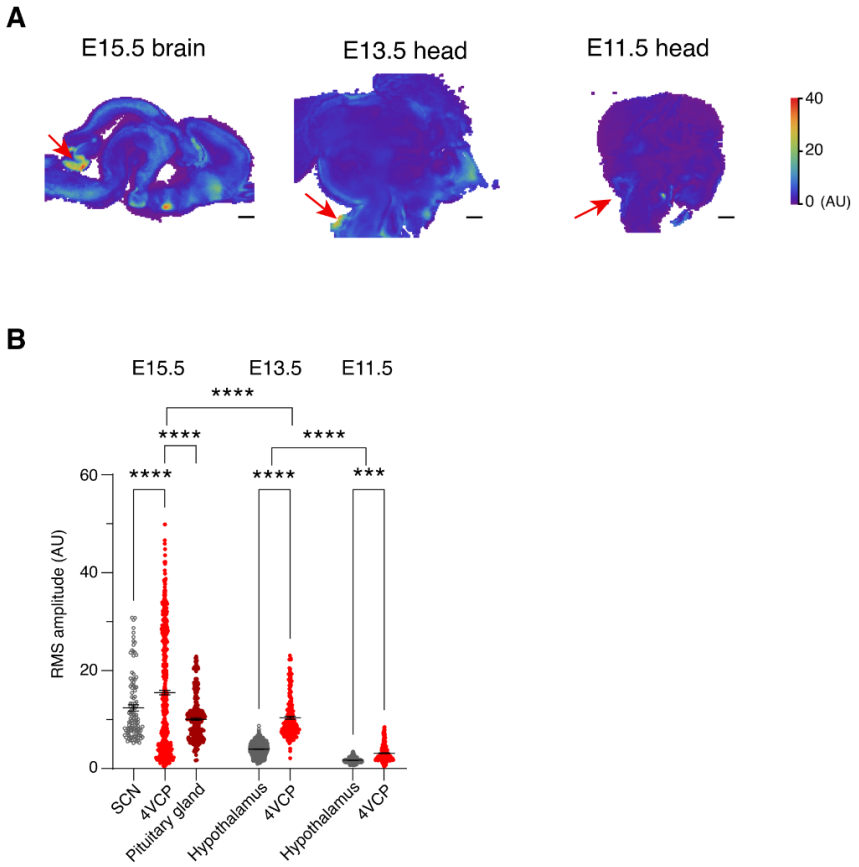

Figure S4. RMS amplitude of PER2::LUC in whole-brain slices at E15.5, E13.5, and E11.5. (**A**) Single-cell level RMS amplitude maps of brain or head slices from E15.5 (left), E13.5 (middle), and E11.5 (right) PER2::LUC embryos. Representative of 3 experiments (5 slices at E15.5, 4 at E13.5, 3 at E11.5). Red arrows indicate the 4VCP. (**B**) RMS amplitude per ROI by brain region within the same slice: SCN (or hypothalamus), 4VCP, and pituitary gland at E15.5, E13.5, and E11.5. One-way ANOVA ($F(6,3911) = 382.5$, $p < 0.0001$) followed by Tukey's post hoc test (****$p < 0.0001$; ***$p < 0.001$; ns: not significant). Error bars: mean ± SEM from one representative slice per stage, after outlier exclusion. Scale bar: 500 µm.

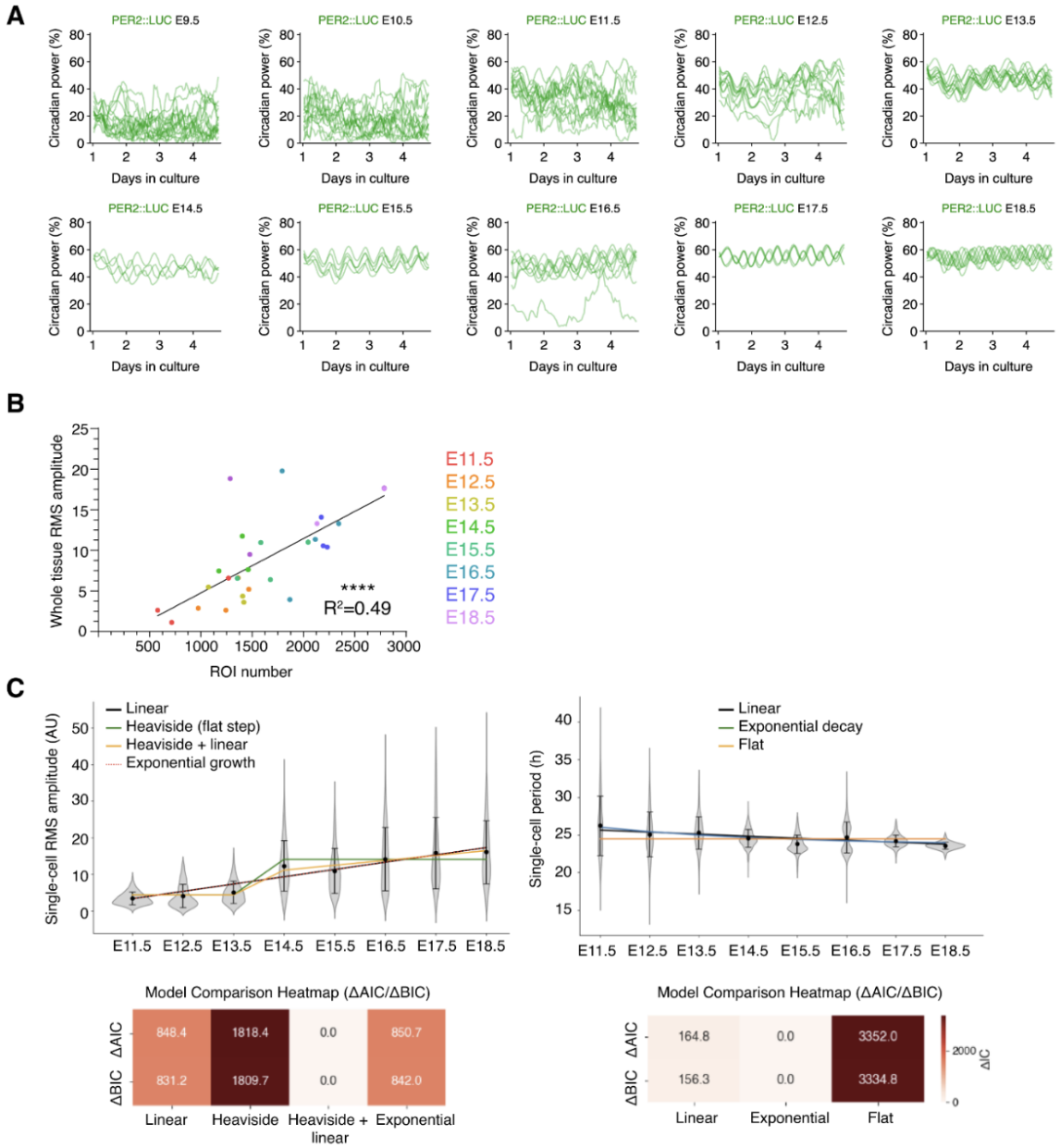

Figure S5. Emergence of significant PER2::LUC circadian power in the 4VCP and relationship between whole-tissue amplitude and cell number. (**A**) Circadian power of individual PER2::LUC 4VCP explants, each line representing one explant. By E12.5, most circadian power trajectories exceed the 20% detection threshold. (**B**) Linear correlation between whole-tissue RMS amplitude and the number of ROIs classified as cells in the embryonic 4VCP across embryonic development (R^2 = 0.49; ****p < 0.0001). The line shows ordinary least-squares fit. (**C**) Model comparison supporting SNIC-like dynamics in single-cell imaging data. Amplitude (left) and period (right) across stages, fitted with candidate models. Heatmaps (bottom) identify the best-fitting model using Akaike Information Criterion

(AIC) and Bayesian Information Criterion (BIC) differences (ΔAIC/ΔBIC) relative to the best model (0 = best; lower = better).

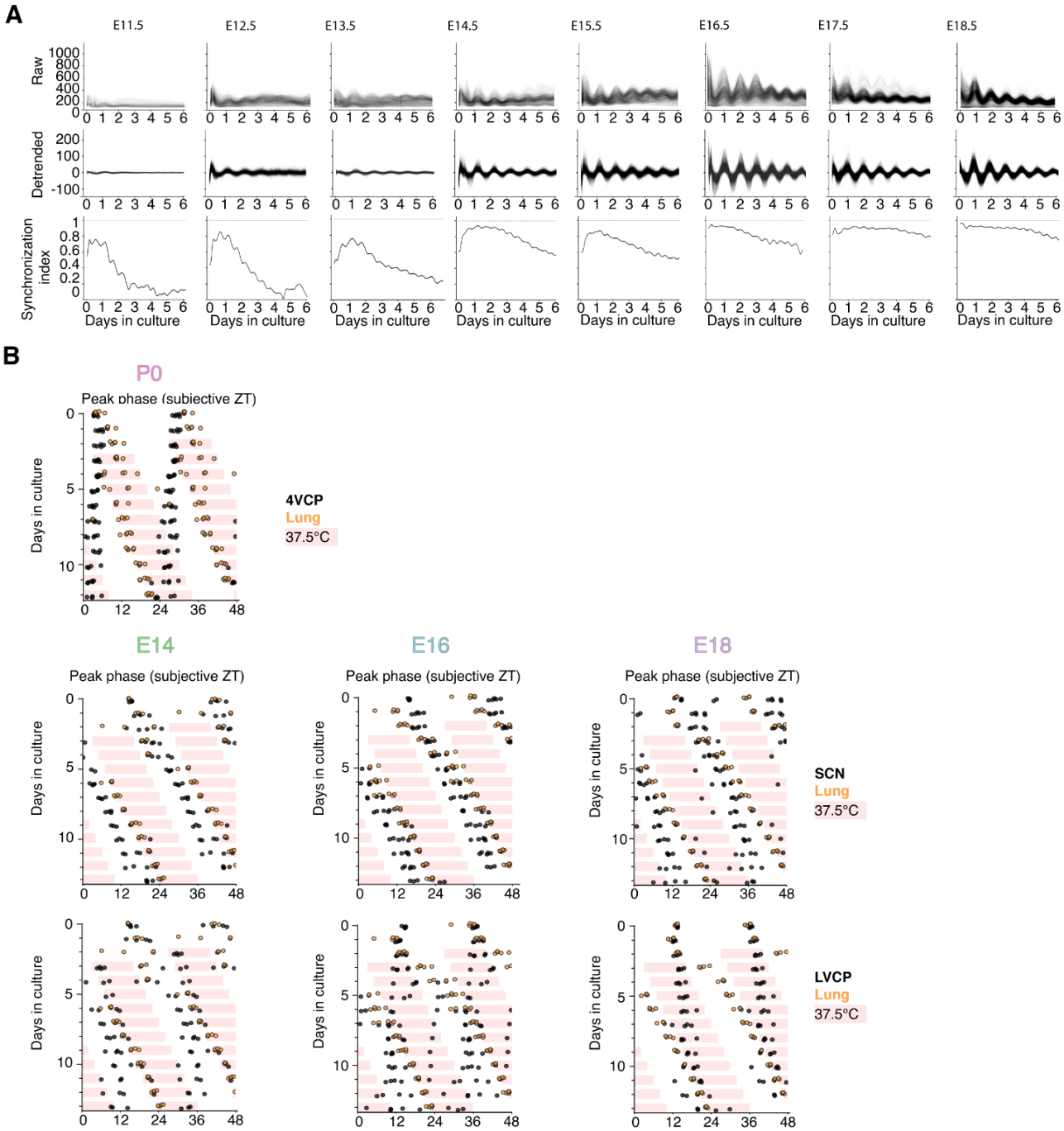

Figure S6. 4VCP cellular synchrony across development and sensitivity of the embryonic SCN and LVCP to a 0.5 °C temperature cycle. (**A**) Raw (top) and detrended (middle) PER2::LUC signals from single-cell imaging of the 4VCP from E11.5 to E18.5, with the corresponding Kuramoto order parameter (bottom). Representative of 3-7 experiments. (**B**) Double-plots of PER2::LUC peak phases from neonatal 4VCPs at P0 (*n* = 4-5; top), embryonic SCN (middle), and LVCPs (bottom) at E14, E16, and E18. Explants were recorded

for 13 days under a 0.5 °C, 26 h cycle following 2 days at 37.0 °C. Lung explants of the corresponding age are shown in orange as an entrainment reference. Pale pink shading indicates the 37.5 °C temperature epochs.

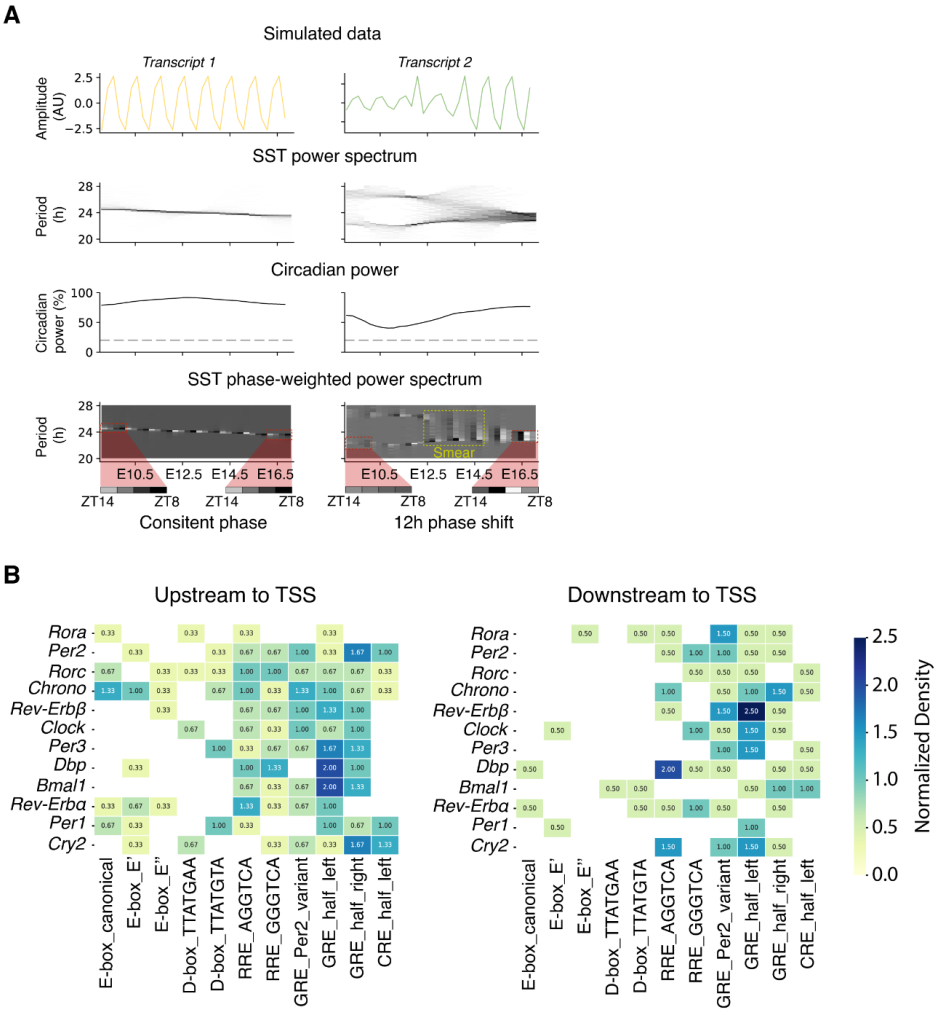

Figure S7. SST-CWT analysis of simulated data and promoter motif density map. (**A**) SST-CWT analysis of simulated time series. Simulated signals for *Transcript 1* (top left) and *Transcript 2* (top right) across developmental time. *Transcript 1* (maternal-like) maintains a stable amplitude and phase; *Transcript 2* (embryonic-like) undergoes amplitude modulation and a 12 h phase shift. SST-CWT power spectrograms highlighting dominant circadian periodicities between 20 and 28 h (upper middle). Circadian power of both simulated transcripts (lower middle). Phase-weighted SST-CWT spectrograms, where color intensity reflects the phase consistency of the dominant period (bottom). Red shading marks early (E9.5) and late (E16.5) windows illustrating phase reorganization; yellow box indicates the spectral smearing interval. (**B**) Normalized density of transcription factor binding motifs for each clock gene.

1103

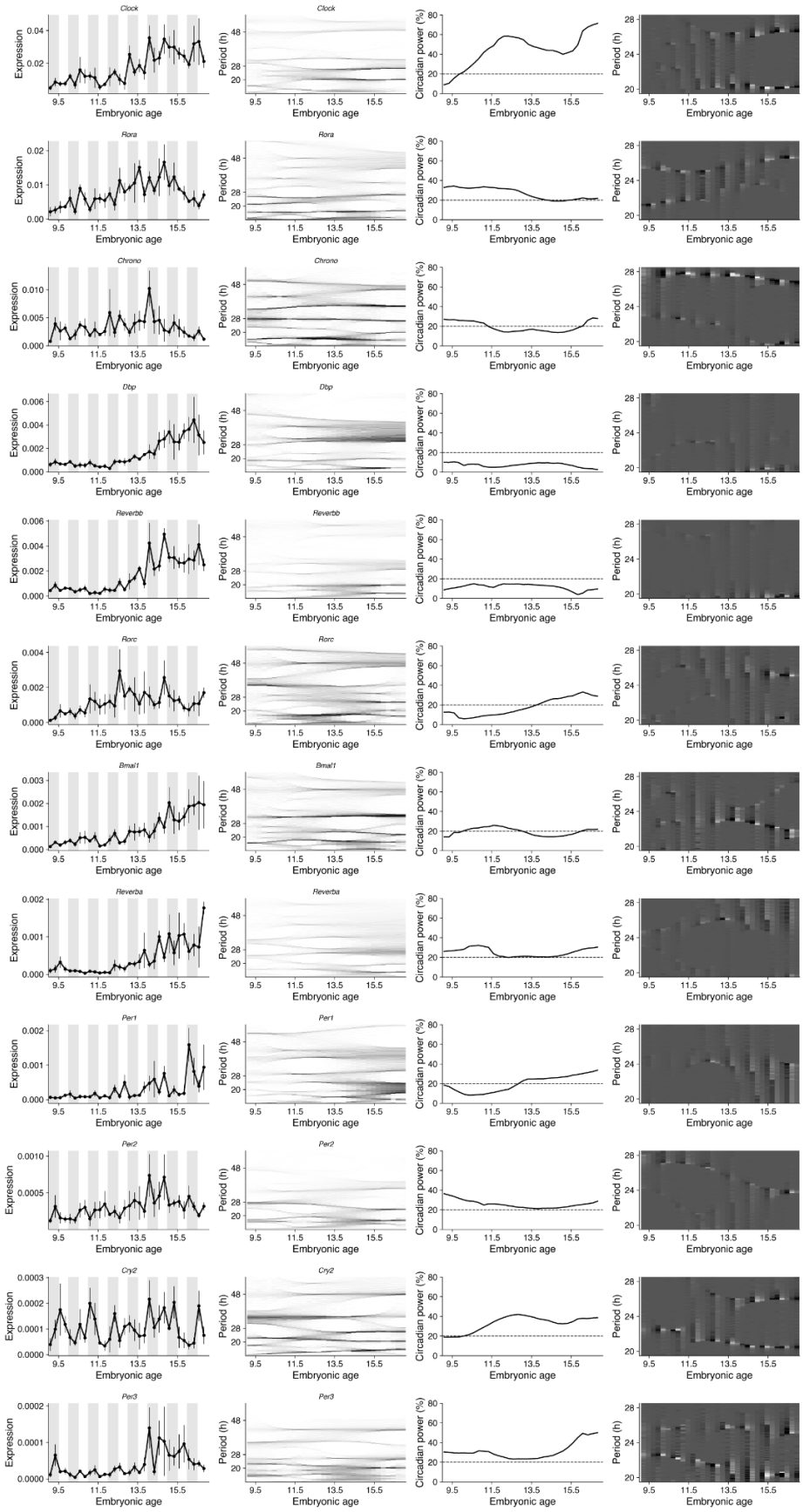
Clock
Rora
Chrono
Dbp
Reverbb
Rorc
Bmal1
Reverba
Per1
Per2
Cry2
Per3
Expression
Period (h)
Circadian power (%)
Embryonic age
9.5
11.5
13.5
15.5

Figure S8. Circadian rhythmicity assessment of embryonic clock genes in the 4VCP. For each gene (rows), four panels are shown from left to right: normalized mRNA expression across embryonic development, sampled every 6 h (ZT2, ZT8, ZT14, ZT20; grey shading indicates the dark phase); SST-CWT spectrogram highlighting dominant circadian periodicities between 20-28 h; circadian power trajectory (dashed line, 20% detection threshold); and phase-weighted SST-CWT spectrogram indicating both dominant period and circadian phase. Error bar: mean ± SEM after outlier exclusion.

1111

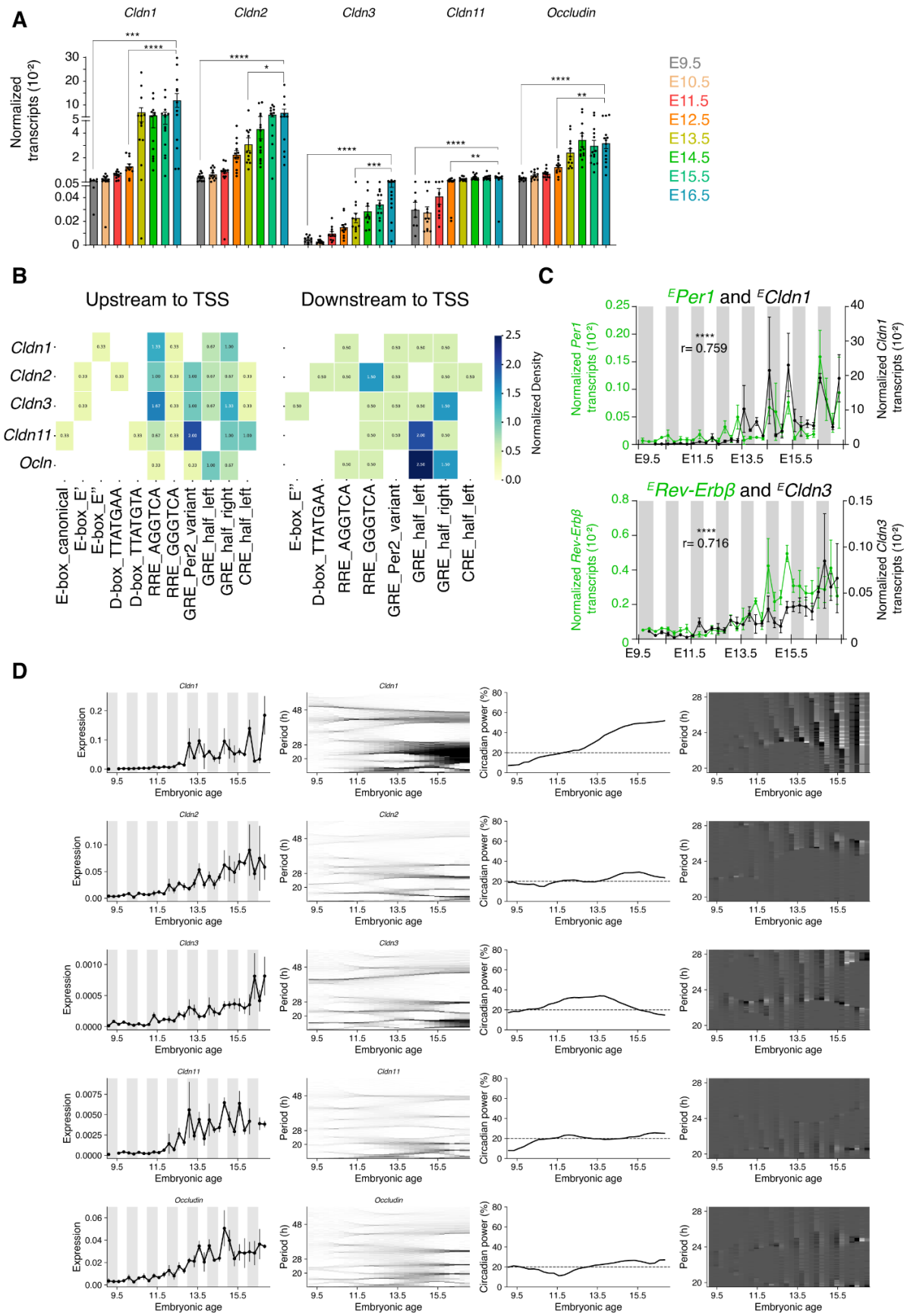
A
Cldn1
Cldn2
Cldn3
Cldn11
Occludin
Normalized transcripts (10²)
E9.5
E10.5
E11.5
E12.5
E13.5
E14.5
E15.5
E16.5
B
Upstream to TSS
Downstream to TSS
Cldn1
Cldn2
Cldn3
Cldn11
Ocln
E-box_canonical
E-box_E'
E-box_E''
D-box_TTATGAA
D-box_TTATGTA
RRE_AGGTCA
RRE_GGGTCA
GRE_Per2_variant
GRE_half_left
GRE_half_right
CRE_half_left
Normalized Density
C
EPer1 and ECldn1
r= 0.759
Normalized Per1 transcripts (10²)
Normalized Cldn1 transcripts (10²)
ERev-Erbβ and ECldn3
r= 0.716
Normalized Rev-Erbβ transcripts (10²)
Normalized Cldn3 transcripts (10²)
E9.5
E11.5
E13.5
E15.5
D
Expression
Period (h)
Circadian power (%)
Embryonic age

1112 **Figure S9. Circadian rhythmicity assessment of embryonic tight junction genes in the**
1113 **embryonic 4VCP.** (**A**) Normalized mRNA abundance of tight junction genes in the embryonic
1114 4VCP from E9.5 to E16.5 (n = 8-25 litters; 3-11 embryos per litter). One-way ANOVA with
1115 Tukey's post hoc test (*$p < 0.05$, **$p < 0.01$, ***$p < 0.001$, ****$p < 0.0001$). (**B**) Normalized
1116 density of transcription factor binding motifs for each tight junction gene. (**C**) Overlaid mRNA
1117 expression of embryonic *Per1* and *Cldn1* (top; $r = 0.759$) and *Rev-Erbβ* and *Cldn3* (bottom; r
1118 $= 0.716$) in the 4VCP across development. Pearson correlation; ****$p < 0.0001$. (**D**) As in Fig.
1119 S8, for tight junction genes. Error bars: mean ± SEM after outlier exclusion.

1120

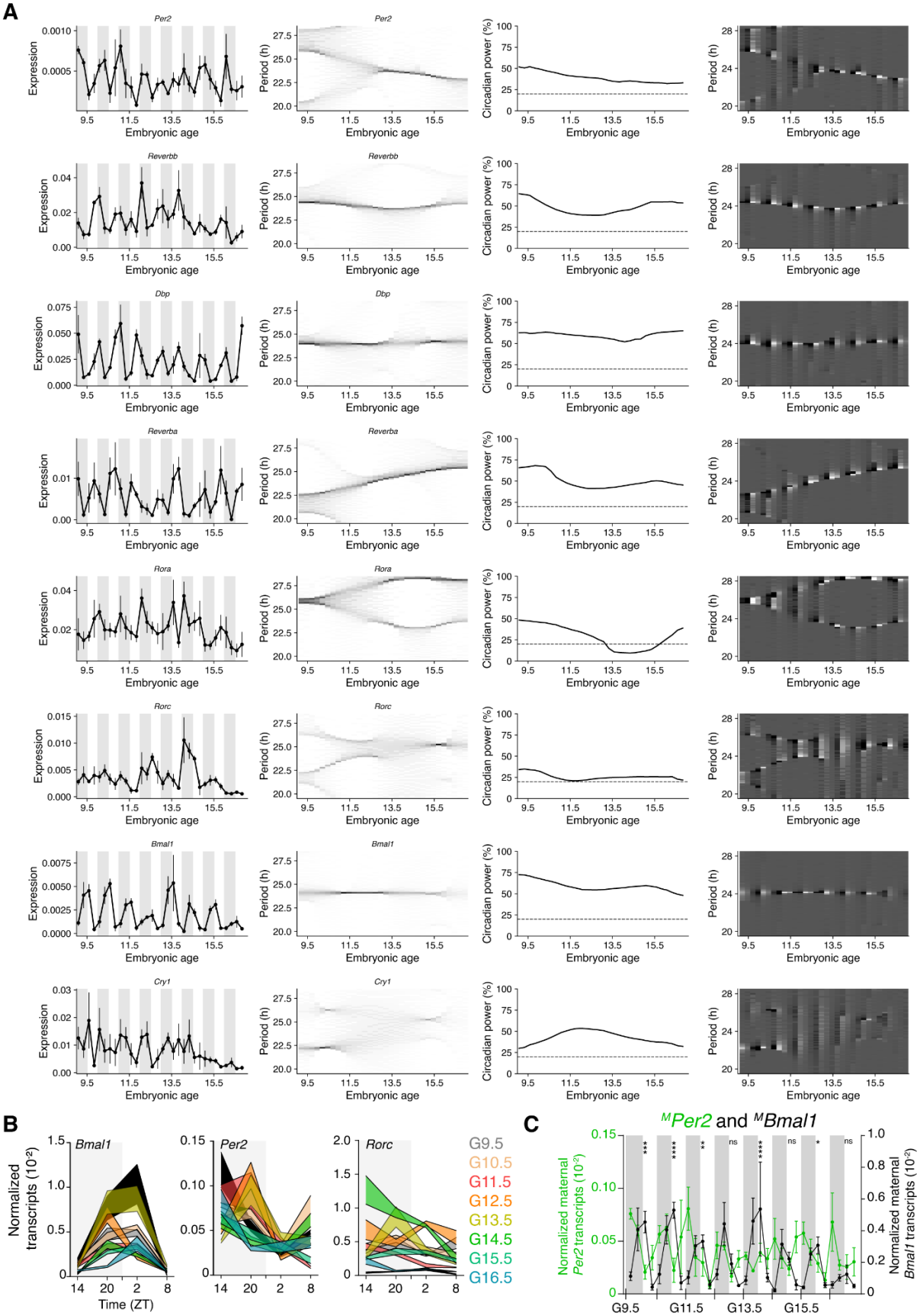
A
Per2
Reverbb
Dbp
Reverba
Rora
Rorc
Bmal1
Cry1
Expression
Period (h)
Circadian power (%)
Embryonic age
B
Normalized transcripts (10⁻²)
Time (ZT)
G9.5
G10.5
G11.5
G12.5
G13.5
G14.5
G15.5
G16.5
C
MPer2 and MBmal1
Normalized maternal Per2 transcripts (10⁻²)
Normalized maternal Bmal1 transcripts (10⁻²)
G9.5
G11.5
G13.5
G15.5

1121 **Figure S10. Circadian rhythmicity assessment of maternal clock genes in the 4VCP.** (**A**)
1122 As in Fig. S8, for maternal clock genes from G9.5 to G16.5. (**B**) Normalized mRNA abundance
1123 of maternal *Bmal1*, *Per2*, and *Rorc*, across ZT from G9.5 to G16.5. Curves show mean ±
1124 SEM from 2-4 dams or 3-5 non-pregnant females. (**C**) Overlaid normalized mRNA expression
1125 of maternal *Per2* (green) and *Bmal1* (black) in the maternal 4VCP across gestation. Two-way
1126 ANOVA comparing *Bmal1* and *Per2* expression across gestational days (time effect:
1127 $F(31,131) = 4.072$, $p < 0.0001$; gene effect: $F(1,131) = 135.9$, $p < 0.0001$), followed by Šidák's
1128 post hoc test at ZT2 (*$p < 0.05$; **$p < 0.01$; ***$p < 0.001$; ****$p < 0.0001$; ns, not significant).
1129 Error bars: mean ± SEM after outlier exclusion.

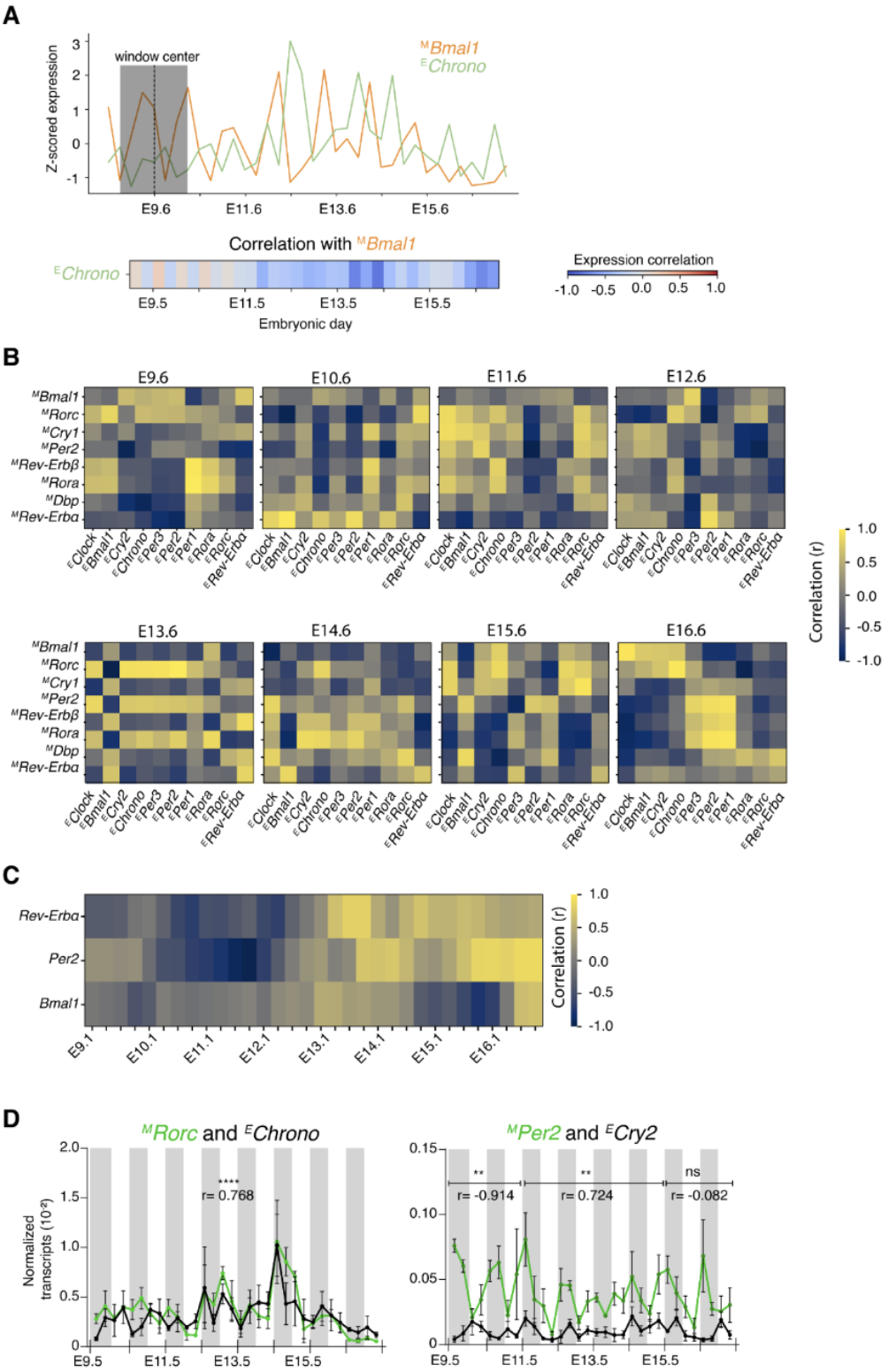

Figure S11. Correlations between maternal and embryonic clock gene expression in the 4VCP. (**A**) Illustration of the sliding-window correlation method between maternal ^{M}*Bmal1* and embryonic ^{E}*Chrono* expression (top). Resulting correlation trajectory between the two

genes in the 4VCP from E9.5 to E16.5 (bottom). (**B**) Pairwise Pearson correlation heatmaps generated using a five-time-point sliding window of transcript levels between maternal and embryonic 4VCP from E9.6 to E16.6. (**C**) Same-gene correlations of *Per2*, *Bmal1*, and *Rev-Erbα* between maternal and embryonic 4VCP from E9.1 to E16.8. (**D**) Overlaid normalized mRNA expression (mean ± SEM) for selected maternal-embryonic pairs: ^{M}*Rorc* vs. ^{E}*Chrono* (left; $r = 0.768$, ****$p < 0.0001$); ^{M}*Per2* vs. ^{E}*Cry2* (right; negatively correlated before E11.5, $r = -0.914$; positively correlated E11.5-E14.5, $r = 0.724$; not correlated E15.5-E16.5, $r = -0.082$). Pearson correlation; *$p < 0.05$; **$p < 0.01$; ****$p < 0.0001$; ns, not significant. Error bars: mean ± SEM after outlier exclusion.

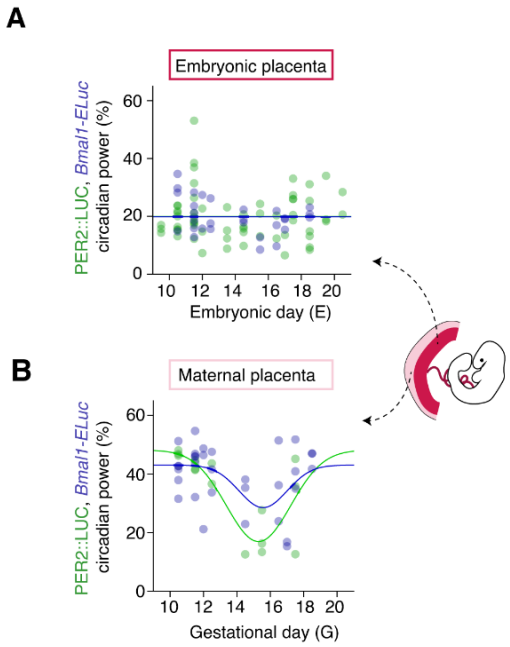

Figure S12. Placental clock robustness during development. (**A**) PER2::LUC and *Bmal1-ELuc* circadian power in the embryonic placenta (dark pink; n = 29 and 68, respectively) from E9.5 to E20.5. (**B**) PER2::LUC and *Bmal1-ELuc* circadian power in the maternal placenta (light pink; n = 15 and 32, respectively) from G10.5 to G18.5. Lines show inverted Gaussian fits. Schematic (right) illustrates the embryonic (dark pink) and maternal (light pink) placental compartments.

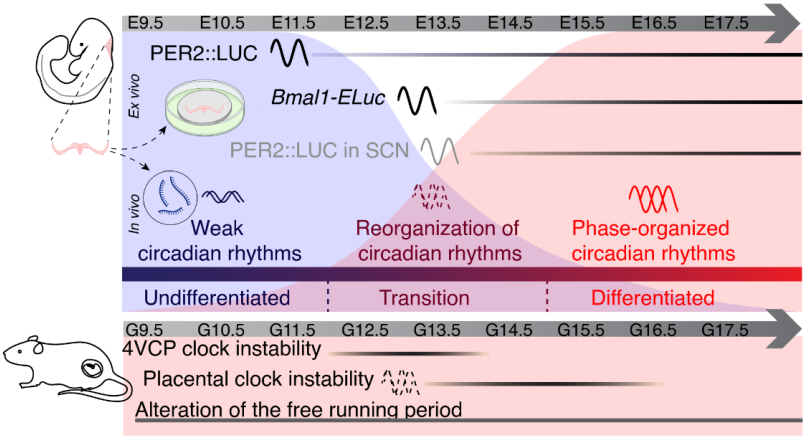

Figure S13. Three differentiation-linked epochs characterize the emergence of the first clock in the embryonic mouse brain. 4VCP is the first brain structure to exhibit autonomous circadian rhythms *ex vivo*, preceding the SCN. Clock assembly is tightly coupled to the tissue's differentiation program and proceeds through three developmental epochs. **(1) Undifferentiated (E9.5-E12):** Clock genes show weak, non-canonical circadian oscillations *in vivo*, despite the absence of an autonomous clock *ex vivo*. **(2) Transition (E12-E15):** As 4VCP cells differentiate, autonomous PER2::LUC oscillations emerge *ex vivo*, while *in vivo* clock gene rhythms undergo transient destabilization, coinciding with mid-gestational instability in the maternal 4VCP clock, placental clock, and maternal free-running behavior. **(3) Differentiated (>E15):** Robust, phase-organized transcriptional circadian oscillations are established *in vivo*. *Ex vivo*, intercellular synchrony strengthens, and the 4VCP matures into a robust oscillator no longer entrainable by low-amplitude maternal temperature cycles.

1163 **Supplementary Movies**
1164

1165 **Movie S1.** Time-lapse of PER2::LUC bioluminescence in an E15.5 sagittal brain slice.
1166 Circadian rhythms are detected in both the SCN and the 4VCP. Elapsed time (h) is shown in
1167 the upper left. Scale bar: 500 μm.
1168
1169 **Movie S2.** Time-lapse of PER2::LUC bioluminescence in an E13.5 sagittal head slice. A
1170 circadian rhythm is detected only in the 4VCP. Elapsed time (h) is shown in the upper left.
1171 Scale bar: 500 μm.
1172
1173 **Movie S3.** Time-lapse of PER2::LUC bioluminescence in an E11.5 sagittal head slice.
1174 PER2::LUC signal is present in the 4VCP region, but no circadian rhythm is detected. Elapsed
1175 time (h) is shown in the upper left. Scale bar: 500 μm.
1176
1177 **Movie S4.** Time-lapse of PER2::LUC bioluminescence in an isolated E13.5 4VCP explant. An
1178 autonomous circadian rhythm is evident *ex vivo*. Elapsed time (h) is shown in the upper left.
1179 Scale bar: 500 μm.